

# Parallel three-dimensional simulations of quasi-static elastoplastic solids. Part II: Coordinate transformations

Nicholas M. Boffi<sup>a</sup>, Chris H. Rycroft<sup>a,b</sup>

<sup>a</sup>*Paulson School of Engineering and Applied Sciences, Harvard University, Cambridge, MA 02139*

<sup>b</sup>*Computational Research Division, Lawrence Berkeley Laboratory, Berkeley, CA 94720*

---

## Abstract

In this two-part paper, we extend to three dimensions a new projection method for simulating hypo-elastoplastic solids in the quasi-static limit. The method is based on a surprising mathematical correspondence to the incompressible Navier–Stokes equations, where the projection method of Chorin (1968) is an established numerical technique. In both parts, we explore the method through numerical simulation of a three-dimensional continuum-level elastoplastic model of a bulk metallic glass, based on the shear transformation zone (STZ) theory of amorphous plasticity.

Here in part II, we present a variation of the projection method based on a coordinate transformation that enables the implementation of boundary conditions through deformation of the grid itself. By considering physically equivalent situations, we show that the original quasi-static method and the transformed method agree up to small differences in discretization errors that shrink as the grid spacing is decreased. We demonstrate how this formalism can be used to implement several interesting cases with ease, such as Lees–Edwards boundary conditions commonly used in molecular-dynamics simulations, and pure shear boundary conditions.

*Keywords:* fluid mechanics, projection method, plasticity, elastoplasticity

---

## 1. Introduction to Part II

In part I [1], we developed a projection method for continuum-level simulation of three-dimensional hypo-elastoplastic solids in the quasi-static limit. We applied the method to study deformation and shear banding in bulk metallic glasses (BMGs), using the shear transformation zone (STZ) theory of amorphous plasticity [2, 3, 4]. The focus of part I was to understand shear banding seen in laboratory tests, where a macroscopic, continuum-level model is applicable.

An alternative approach to studying deformation and failure is to use molecular dynamics (MD), whereby atoms or molecules are individually simulated according to Newton’s laws [5].

---

*Email addresses:* boffi@g.harvard.edu (Nicholas M. Boffi), chr@seas.harvard.edu (Chris H. Rycroft)

MD simulations are widely used in many contexts [6, 7, 8, 9], and several open-source software packages such as LAMMPS [10, 11] and GROMACS [12] are available. MD simulations provide a detailed view of the material physics and are able to capture discrete particle-level effects [13, 14] that are frequently absent in a continuum simulation. However, MD simulations are computationally expensive, meaning that it is usually only possible to simulate microscopic material samples. Furthermore, since the simulations must resolve rapid interaction timescales between particles, the applied deformation rates in MD are often orders of magnitude larger than deformation rates in laboratory tests.

The advantage of continuum simulation over MD is the ability to scale to large system sizes and long times. However, continuum theories require one significant approximation: the transition to the continuum involves an averaging, or coarse-graining, procedure over a small length scale  $l$ , typically on the order of a few atomic radii. The volume enclosed in  $l^d$  where  $d$  is the system dimension is typically referred to as a representative volume element (RVE), and the fundamental assumption of a continuum theory is that the discrepancy between the relevant system variables and their average throughout an RVE can be neglected [15, 16]. Furthermore, the coarse-graining procedure often introduces internal state variables such as the effective temperature field  $\chi$  in the STZ theory, and physically accurate initial conditions for such internal variables can be difficult to construct, or even understand physically [17].

A coarse-graining procedure that remains faithful to the microscopic physics is fundamental in constructing a continuum theory capable of accurately capturing physical phenomena predicted by microscopic theories. This process is difficult in general, and has been most successful when tailored to specific phenomena. Some equilibrium systems are amenable to statistical mechanics-based rigorous approaches [18, 19], and some so-called “mesoscale models” have had success in coarse-grained modeling [20, 21, 22, 23]. The first of these strategies do not generalize to out-of-equilibrium systems such as amorphous systems driven by shear. The second are difficult to connect to experiments for amorphous systems, and typically make no connection to the thermodynamics underlying amorphous plasticity.

The lack of applicability of standard coarse-graining methods to amorphous solids mandates a well-defined approach for comparison of MD and continuum-scale simulations. Since MD simulations simulate microscopic domains, it is difficult to apply deformation via moving walls, since simulation data may be affected by finite-size effects. Instead, the standard approach is to apply periodic boundary conditions, but manipulate the periodic images of the primary simulation domain to achieve different applied deformation. For example, in three-dimensional Lees–Edwards boundary conditions, the periodic images have a horizontal velocity proportional to their  $z$  position in order to impose simple shear [24] (Fig. 1(a)). The Kraynik–Reinelt boundary conditions [25, 26, 27, 28], plus a recent generalization by Dobson [29], use a combination of moving periodic images and domain remapping in order to simulate different extensional flows.

To systematically match to MD, it would be ideal to recreate these types of boundary conditions exactly, but this poses some numerical challenges. Consider the Lees–Edwards boundary conditions and suppose that the primary simulation domain is represented on a rectangular grid. Then, because the periodic images are moving, their grids will generally not

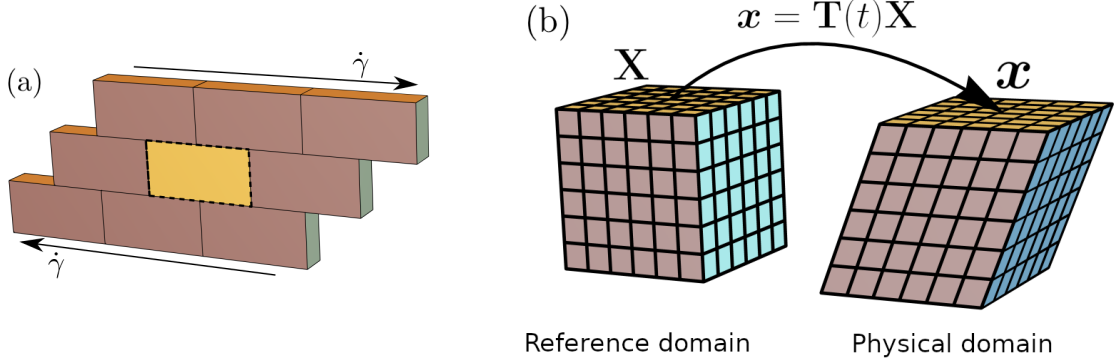


Figure 1: (a) Lees-Edwards boundary conditions. The system of interest is shown in yellow and outlined in dashed black lines. Periodic copies of the system above and below are set to move with a specific velocity, imposing a specific strain rate  $\dot{\gamma}$  on the system. (b) A graphical depiction of a domain transformation  $\mathbf{T}(t)$  that maps a fixed reference domain  $\mathbf{X}$  to a sheared physical domain  $\mathbf{x}$ .

align with primary domain. This could be handled numerically via interpolation, but grid points near the boundary will incur different discretization errors. Given that the nucleation and growth of shear banding may be driven by subtle features, this extra source of error may be a significant problem. Furthermore, the quasi-static projection method requires solving a large linear system on the primary domain. When the periodic images are displaced, the linear system has a more complex structure of connectivity, and is no longer ideal for applying the standard geometric multigrid method [30, 31]. Recently, the two-dimensional projection method of Rycroft *et al.* [32] was compared systematically to Lees-Edwards MD simulations [33], but the continuum simulation applied shear via moving walls, leading to a mismatch in boundary conditions that needed to be accounted for in the analysis.

In this work, we introduce a coordinate transformation framework that allows MD boundary conditions to be recreated precisely. It is based on an abstract linear mapping  $\mathbf{T}(t)$  from a *reference frame* to the *physical frame* (Fig. 1(b)). Lees-Edwards conditions can be implemented in the continuum setting by imposing shear through a transformation and enforcing periodic boundary conditions in all directions. In addition to Lees-Edwards boundary conditions, the transformation framework is flexible, and enables simple implementation of otherwise difficult boundary conditions, such as pure shear.

Part II is entirely concerned with the coordinate transformation framework, and can mostly be read independently of part I. Though the projection algorithm presented here is an extension of the method developed in part I, it is derived in full detail in the reference frame here in part II. The reader may find it simpler to become familiar with the projection algorithm from part I before considering the transformations here, but this is not a prerequisite. The STZ model is a test case for our algorithm, and its physical details are discussed only in part I, though the equations it provides for the plastic rate of deformation tensor are still employed here and briefly reviewed in the following section.

### 1.1. Summary of part I and review of the STZ theory

We consider an elastoplastic material with Cauchy stress tensor  $\boldsymbol{\sigma}(\mathbf{x}, t)$  and velocity field  $\mathbf{v}(\mathbf{x}, t)$ . We denote by  $\mathbf{L} = \nabla \mathbf{v}$  the velocity gradient tensor and  $\mathbf{D} = \frac{1}{2}(\mathbf{L} + \mathbf{L}^\top)$  the rate of deformation tensor. We adopt the framework of hypo-elastoplasticity, which assumes the rate of deformation tensor can be additively decomposed into elastic and plastic parts as  $\mathbf{D} = \mathbf{D}^{\text{el}} + \mathbf{D}^{\text{pl}}$ . Writing linear elasticity in rate form yields

$$\frac{\mathcal{D}\boldsymbol{\sigma}(\mathbf{x}, t)}{\mathcal{D}t} = \mathbf{C} : (\mathbf{D} - \mathbf{D}^{\text{pl}}) \quad (1)$$

where  $\mathbf{C}$  is the stiffness tensor. For simplicity, the material is taken to be isotropic and homogeneous, so that  $C_{ijkl} = \lambda \delta_{ij} \delta_{kl} + \mu (\delta_{ik} \delta_{jl} + \delta_{il} \delta_{jk})$  with  $\lambda$  the first Lamé parameter and  $\mu$  the shear modulus. The time derivative in Eq. 1 is the Truesdell derivative,  $\frac{\mathcal{D}\boldsymbol{\sigma}}{\mathcal{D}t} = \frac{d\boldsymbol{\sigma}}{dt} - \mathbf{L}^\top \boldsymbol{\sigma} - \boldsymbol{\sigma} \mathbf{L} + \text{tr}(\mathbf{L})\boldsymbol{\sigma}$ ,<sup>1</sup> with  $\frac{d}{dt} = \frac{\partial}{\partial t} + \mathbf{v} \cdot \nabla$  denoting the advective derivative. The velocity field satisfies a continuum-scale Newton's second law,

$$\rho \frac{d\mathbf{v}}{dt} = \nabla \cdot \boldsymbol{\sigma}, \quad (2)$$

with  $\rho$  the material density.

A family of projection methods for the quasi-static limit of the hypo-elastoplastic equations Eqs. 1 & 2 was developed in part I. This development was based on a correspondence with the Navier-Stokes equations for incompressible fluid flow, and extends previous two-dimensional work [32]. In the quasi-static limit, Eq. 2 is replaced with the quasi-static constraint on the stress field,

$$\nabla \cdot \boldsymbol{\sigma} = \mathbf{0}. \quad (3)$$

The projection methods developed in part I proceed via a two-step method. They enable solving Eq. 1 subject to constraint Eq. 3, despite the lack of evolution equation for the velocity field  $\mathbf{v}$  in this limit. A numerical implementation of an example projection method was presented, and it was quantitatively compared to a simple explicit forward Euler discretization of Eqs. 1 & 2 in three dimensions. Several numerical examples from the shear transformation zone (STZ) model of amorphous plasticity with uniquely three-dimensional dynamics were considered. For completeness, we now present the necessary equations from the STZ theory. The reader interested in its physical details is encouraged to read part I or a recent review [1, 35].

We define the deviatoric stress tensor  $\boldsymbol{\sigma}_0 = \boldsymbol{\sigma} - \frac{1}{3} \text{tr}(\boldsymbol{\sigma}) \mathbf{I}$ . The total rate of plastic deformation tensor is proportional to the deviatoric stress,  $\mathbf{D}^{\text{pl}} = D^{\text{pl}} \frac{\boldsymbol{\sigma}_0}{\bar{s}}$ , where  $\bar{s}^2 = \frac{1}{2} \boldsymbol{\sigma}_{0,ij} \boldsymbol{\sigma}_{0,ij}$

---

<sup>1</sup>It is noted in part I that this expression is typically presented with  $\mathbf{L}$  transposed with respect to the definition here. We adopt the convention that  $(\nabla \mathbf{f})_{ij} = \partial_i f_j$  (partial derivatives go row-wise in gradients of vector fields) for any field  $\mathbf{f}$ ; the typical Truesdell derivative definition uses a convention where partial derivatives go column-wise [34]. The usual appearance of  $\mathbf{L}$  in the Truesdell derivative is the Jacobian of the velocity field, which is formally the transpose of our definition of  $\nabla \mathbf{f}$ . The transformed formalism here involves both Jacobians and vector field gradients, and for physically consistent answers it is necessary to make this distinction.

is a local scalar measure of the total deviatoric stress. The STZ theory provides the magnitude of the plastic rate of deformation as

$$\tau_0 D^{\text{pl}} = e^{-e_z/k_B \chi} e^{-\Delta/k_B T} \cosh\left(\frac{\Omega \epsilon_0 \bar{s}}{k_B T}\right) \left(1 - \frac{s_Y}{\bar{s}}\right). \quad (4)$$

$\tau_0$  is a molecular vibration timescale,  $e_z$  is a typical STZ formation energy,  $k_B$  the Boltzmann constant,  $T$  is the thermodynamic temperature,  $\Delta$  is a typical energetic barrier for a transition,  $\Omega$  is a typical STZ volume, and  $\epsilon_0$  is a typical local strain. The effective temperature satisfies a heat equation [36, 37, 38, 39, 40]

$$c_0 \frac{d\chi}{dt} = \frac{(\mathbf{D}^{\text{pl}} : \boldsymbol{\sigma}_0)}{s_Y} (\chi_\infty - \chi) + l^2 \nabla \cdot (D^{\text{pl}} \nabla \chi). \quad (5)$$

The interdependence of Eqs. 4 & 5 enables the development of shear bands through a positive feedback mechanism, as increasing one of  $\chi$  or  $D^{\text{pl}}$  also leads to an increase in the other [37, 39].

## 2. Coordinate transformations

Let  $\mathbf{T}(t)$  denote a time-varying mapping from a reference domain  $\mathbf{X}$  to the physical domain of interest  $\mathbf{x}$  such that

$$\mathbf{x} = \mathbf{T}\mathbf{X}, \quad (6)$$

as shown in Fig. 1(b). Here,  $\mathbf{X} \in [a_X, b_X] \times [a_Y, b_Y] \times [a_Z, b_Z]$ . Capital letters denote quantities in the reference frame and lower case letters denote quantities in the physical frame.  $\nabla_{\mathbf{X}}$  and  $\nabla_{\mathbf{x}}$  denote spatial differentiation in the reference and untransformed frame, respectively. We emphasize that  $\mathbf{X}$  exists in a fixed frame on which the quasi-static hypo-elastoplastic equations will be solved, and not in the Lagrangian frame of coordinates. To clarify this point, let  $\mathcal{R} = (\mathcal{X}, \mathcal{Y}, \mathcal{Z})$  denote a set of fixed Lagrangian coordinates. For an Eulerian frame  $(x, y, z)$ , we define the Eulerian displacements,

$$u_i = x_i - \mathcal{R}_i. \quad (7)$$

We then define the Eulerian velocities  $v_i = \frac{\partial u_i}{\partial t}|_{\mathcal{R}}$ . The same procedure can be performed in the physical frame. We first define the physical displacements,

$$\mathbf{u} = \mathbf{T}\mathbf{X} - \mathcal{R}. \quad (8)$$

Taking a time derivative of both sides of Eq. 8 at fixed Lagrangian coordinates  $\mathcal{R}$ , we arrive at an expression for the physical velocity,

$$\mathbf{v} = \frac{\partial \mathbf{T}}{\partial t} \mathbf{X} + \mathbf{T}\mathbf{V}. \quad (9)$$

Above, we have identified the transformed velocity  $\mathbf{V} = \frac{\partial \mathbf{X}}{\partial t}|_{\mathcal{R}}$ . Equation 9 can be used to compute the *physical* velocity  $\mathbf{v}$  from the *transformed* velocity  $\mathbf{V}$ , if  $\mathbf{V}$  is known. By inversion, it can also be used as a definition of the transformed velocity,

$$\mathbf{V} = \mathbf{T}^{-1} \left( \mathbf{v} - \frac{\partial \mathbf{T}}{\partial t} \mathbf{X} \right). \quad (10)$$

Using the chain rule, spatial derivatives are transformed as

$$\nabla_{\mathbf{X}} = \mathbf{T}^{-\top} \nabla_{\mathbf{x}}. \quad (11)$$

Taking an advective time derivative of Eq. 10, using Eq. 2 for  $\dot{\mathbf{v}}$ , and transforming physical spatial derivatives to transformed spatial derivatives, the transformed velocity evolves according to the transformed generalization of Newton's second law,

$$\frac{\partial \mathbf{V}}{\partial t} = -(\mathbf{V} \cdot \nabla_{\mathbf{X}}) \mathbf{V} + \frac{\partial \mathbf{T}^{-1}}{\partial t} \mathbf{T} \mathbf{V} + \mathbf{T}^{-1} \left( \mathbf{T}^{-\top} \nabla_{\mathbf{X}} \cdot (\mathbf{T} \Sigma \mathbf{T}^{\top}) - \frac{\partial^2 \mathbf{T}}{\partial t^2} \mathbf{X} - \frac{\partial \mathbf{T}}{\partial t} \mathbf{V} \right). \quad (12)$$

In Eq. 12, we have rewritten the advective derivative  $\frac{\partial}{\partial t} + \mathbf{v} \cdot \nabla_{\mathbf{x}} = \frac{\partial}{\partial t} + \mathbf{V} \cdot \nabla_{\mathbf{X}}$ . The derivation of this for an arbitrary transformation  $\mathbf{T}(t)$  is shown in [Appendix A](#).

We define the transformed stress tensor via the contravariant pullback,

$$\Sigma = \mathbf{T}^{-1} \boldsymbol{\sigma} \mathbf{T}^{-\top}. \quad (13)$$

We take an identical approach to derive an evolution equation for  $\Sigma$ , now using the linear elastic relation in Eq. 1. Taking an advective time derivative of the definition of  $\Sigma$ , the transformed stress then obeys the transformed generalization of the linear elastic constitutive law. After expansion of the Truesdell rate,

$$\begin{aligned} \frac{\partial \Sigma}{\partial t} = & -(\mathbf{V} \cdot \nabla_{\mathbf{X}}) \Sigma - \text{tr}(\mathbf{L}) \Sigma + \Sigma (\mathbf{T}^{\top} \mathbf{L}^{\top} \mathbf{T}^{-\top}) + (\mathbf{T}^{-1} \mathbf{L} \mathbf{T}) \Sigma \\ & + \mathbf{T}^{-1} \left( \mathbf{C} : (\mathbf{D} - \mathbf{D}^{\text{pl}}) - \frac{\partial \mathbf{T}}{\partial t} \Sigma \mathbf{T}^{\top} - \mathbf{T} \Sigma \frac{\partial \mathbf{T}^{\top}}{\partial t} \right) \mathbf{T}^{-\top}. \end{aligned} \quad (14)$$

In Eq. 14,  $\mathbf{L}$  and  $\mathbf{D}$  refer to the physical quantities.  $\mathbf{L}$  can be computed in terms of the transformed variables as

$$\mathbf{L} = \mathbf{T}^{-\top} \frac{\partial \mathbf{T}}{\partial t} + \mathbf{T}^{-\top} \mathbf{T} \nabla_{\mathbf{x}} \mathbf{V}, \quad (15)$$

and  $\mathbf{D} = \frac{1}{2} (\mathbf{L} + \mathbf{L}^{\top})$  can be computed in terms of entirely transformed variables via Eq. 15. For brevity, we do not substitute Eq. 15 into Eq. 14.

$\mathbf{D}^{\text{pl}} = D^{\text{pl}} \frac{\boldsymbol{\sigma}_0}{s}$  appears in Eq. 14, and its form depends on the plasticity model through the constant  $D^{\text{pl}}$ . As reviewed in Sec. 1.1, the STZ theory provides an expression given by Eq. 4.  $\mathbf{D}^{\text{pl}}$  is defined and must be computed in terms of the physical deviatoric stress  $\boldsymbol{\sigma}_0$ . In line with the definition of  $\Sigma$ , we can apply the contravariant pullback to  $\boldsymbol{\sigma}_0$  and write

$$\mathbf{T}^{-1} \boldsymbol{\sigma}_0 \mathbf{T}^{-\top} = \Sigma - \frac{1}{3} (\mathbf{T}^{-1} \text{tr} (\mathbf{T} \Sigma \mathbf{T}^{\top}) \mathbf{T}^{-\top}) \mathbf{I}. \quad (16)$$

Using the natural definition  $\Sigma_0 = \Sigma - \frac{1}{3} \text{tr}(\Sigma) \mathbf{I}$  and solving for  $\sigma_0$ , we can rewrite Eq. 16 as

$$\sigma_0 = \mathbf{T} \Sigma_0 \mathbf{T}^\top + \frac{1}{3} (\mathbf{T} \text{tr}(\Sigma) \mathbf{T}^\top - \text{tr}(\mathbf{T} \Sigma \mathbf{T}^\top)) \mathbf{I}. \quad (17)$$

Equation 17 enables the computation of  $\sigma_0$  entirely in terms of transformed quantities. We compute  $\bar{s}$  by first computing the entire tensor  $\sigma_0$  using Eq. 17 and then compute its Frobenius norm.

The equation for the effective temperature must also be transformed, though we do not define a transformed effective temperature. This can be accomplished by transforming the derivatives,

$$c_0 \frac{\partial \chi}{\partial t} = -c_0 (\mathbf{V} \cdot \nabla_{\mathbf{x}}) \chi + \frac{(\mathbf{D}^{\text{pl}} : \sigma_0)}{s_Y} (\chi_\infty - \chi) + l^2 \mathbf{T}^{-\top} \nabla_{\mathbf{x}} \cdot (D^{\text{pl}} \mathbf{T}^{-\top} \nabla_{\mathbf{x}} \chi). \quad (18)$$

For brevity,  $\mathbf{D}^{\text{pl}}$ ,  $\sigma_0$  and  $D^{\text{pl}}$  refer to the physical quantities in Eq. 18 and must be computed in terms of the transformed variables in an implementation. Transformation of the diffusive term ensures that diffusion occurs in the physical frame despite being implemented in the reference frame.

The benefit of using a Truesdell derivative becomes apparent upon consideration of specific cases of Eqs. 12 & 14. A particular case of interest is simple shear, given the immediate application to implementation of Lees–Edwards boundary conditions. This physical situation is described by the transformation

$$\mathbf{T} = \begin{pmatrix} 1 & 0 & u_b t \\ 0 & 1 & 0 \\ 0 & 0 & 1 \end{pmatrix}, \quad (19)$$

with  $u_b$  a boundary shear velocity. Restriction to a two-dimensional plane-strain formulation reveals that the components of Eqs. 12 & 14 retain their original form with untransformed quantities replaced by transformed quantities, in addition to several new terms proportional to powers of  $u_b t$ .

### 2.1. Projection method

We now formulate a two-step projection method in the reference frame. This method enables solving for  $\mathbf{V}$  and  $\Sigma$  subject to the constraint that  $\nabla_{\mathbf{x}} \cdot \sigma = \mathbf{0}$ . In the first step, the  $\mathbf{C} : \mathbf{D}$  term in Eq. 14 is neglected to compute the intermediate transformed stress  $\Sigma^*$ ,

$$\begin{aligned} \frac{\Sigma^* - \Sigma^n}{\Delta t} = & -(\mathbf{V}^n \cdot \nabla_{\mathbf{x}}) \Sigma^n - \text{tr}(\mathbf{L}^n) \Sigma^n + \Sigma^n ((\mathbf{T}^\top)^n (\mathbf{L}^\top)^n (\mathbf{T}^{-\top})^n) \\ & + ((\mathbf{T}^{-1})^n \mathbf{L}^n \mathbf{T}^n) \Sigma^n - (\mathbf{T}^{-1})^n \mathbf{C} : (\mathbf{D}^{\text{pl}})^n \\ & - (\mathbf{T}^{-1})^n \left( \left( \frac{\partial \mathbf{T}}{\partial t} \right)^n \Sigma^n (\mathbf{T}^\top)^n - \mathbf{T}^n \Sigma^n \left( \frac{\partial \mathbf{T}^\top}{\partial t} \right)^n \right) (\mathbf{T}^{-\top})^n. \end{aligned} \quad (20)$$

If the transformed velocity at the next timestep  $\mathbf{V}^{n+1}$  were known, we could compute  $\mathbf{L}^{n+1}$  via Eq. 15, compute  $\mathbf{D}^{n+1} = \frac{1}{2}(\mathbf{L}^\top + \mathbf{L})$ , and complete the transformed Euler step via

$$\boldsymbol{\Sigma}^{n+1} = \boldsymbol{\Sigma}^* + \Delta t (\mathbf{T}^{-1})^n (\mathbf{C} : \mathbf{D}^{n+1}) (\mathbf{T}^{-\top})^n. \quad (21)$$

To compute this correction, we need to use the physical constraint Eq. 3. As shown in part I, the equivalent of Eq. 20 in the physical frame is

$$\frac{\boldsymbol{\sigma}^* - \boldsymbol{\sigma}^n}{\Delta t} = (\mathbf{L}^\top)^n \boldsymbol{\sigma}^n + \boldsymbol{\sigma}^n \mathbf{L}^n - \text{tr}(\mathbf{L}^n) \boldsymbol{\sigma}^n - \mathbf{C} : \left( \frac{D^{\text{pl}}}{\bar{s}^n} \boldsymbol{\sigma}_0^n \right), \quad (22)$$

and the equivalent of Eq. 21 is

$$\boldsymbol{\sigma}^{n+1} = \boldsymbol{\sigma}^* + \Delta t (\mathbf{C} : \mathbf{D}^{n+1}). \quad (23)$$

Enforcing that  $\nabla_{\mathbf{x}} \cdot \boldsymbol{\sigma}^{n+1} = \mathbf{0}$  in Eq. 23 leads to a linear system for  $\mathbf{v}$ ,

$$\Delta t \nabla_{\mathbf{x}} \cdot (\mathbf{C} : \mathbf{D}^{n+1}) = -\nabla_{\mathbf{x}} \cdot \boldsymbol{\sigma}^*. \quad (24)$$

From Eqs. 20 & 22, it is clear that  $\mathbf{T}^{-1} \boldsymbol{\sigma}^* \mathbf{T}^{-\top} = \boldsymbol{\Sigma}^*$ . Using this, the right hand side of Eq. 24 transforms according to

$$-\nabla_{\mathbf{x}} \cdot \boldsymbol{\sigma}^* = -\mathbf{T} \nabla_{\mathbf{x}} \cdot \boldsymbol{\Sigma}^*. \quad (25)$$

The left-hand side of Eq. 24 generalizes to

$$\begin{aligned} \frac{\Delta t}{2} \mathbf{T}^{-\top} \nabla_{\mathbf{x}} \cdot \left( \mathbf{C} : \left( \left( \mathbf{T}^{-\top} \frac{\partial \mathbf{T}}{\partial t} + \frac{\partial \mathbf{T}^\top}{\partial t} \mathbf{T}^{-1} \right)^n \right. \right. \\ \left. \left. + (\mathbf{T}^{-\top} \mathbf{T})^n \nabla_{\mathbf{x}} \mathbf{V}^{n+1} + (\nabla_{\mathbf{x}} \mathbf{V}^{n+1})^\top (\mathbf{T}^\top \mathbf{T}^{-1})^n \right) \right). \end{aligned} \quad (26)$$

Equations 25 & 26 form a complicated linear system for the transformed velocity  $\mathbf{V}^{n+1}$ . The appearance of the transformation  $\mathbf{T}$  in front of the gradient operator  $\nabla_{\mathbf{x}}$  ensures that all mixed spatial derivatives of all components of the velocity appear in each row of Eq. 26. Equation 26 is significantly more complex than the linear system in standard, non-transformed quasi-static hypo-elastoplasticity, and is dependent on the specific form of  $\mathbf{T}$ . Nevertheless, it can be solved via standard techniques of linear algebra, and we use the same custom multigrid implementation described in part I to do so. Equations 20, 21, 25, & 26 are discretized on a staggered grid using centered difference stencils in an identical manner to part I.

After spatial discretization of Eq. 26, the linear system is of the form  $\mathbf{A} \mathbf{x} = \mathbf{b}$ .  $\mathbf{b}$  is given in block form by the source term in Eq. 25,  $\mathbf{b}_i = \nabla_{\mathbf{x}} \cdot \boldsymbol{\sigma}^*(\mathbf{X}_i)$ , where the index  $i$  runs over all grid points.  $\mathbf{x}$  is also given in block form, so that  $\mathbf{x}$  contains the stacked values of  $\mathbf{V}$  across all grid points. The matrix  $\mathbf{A}$  is sparse, and its degree of sparsity depends on the specific discretization scheme used. In the staggered centered difference scheme used here, grid point  $(i, j, k)$  only feels the influence of the 27 grid points in the surrounding  $3 \times 3 \times 3$  cube.  $\mathbf{A}$  is most effectively reconstructed using submatrices  $\mathbf{A}_{(k,l,m)}^{(i,j,k)}$ , which give the coefficients of

velocity values  $\mathbf{V}_{(k,l,m)}$  appearing in the linear equation for  $\mathbf{V}_{(i,j,k)}$ . Each matrix  $\mathbf{A}_{(k,l,m)}^{(i,j,k)}$  is symmetric.

A highlight of the transformation methodology is its flexibility and simplicity. Implementation of new boundary conditions, so-long as they can be specified in terms of a transformation  $\mathbf{T}(t)$ , is only as difficult as writing the transformation down. The transformation will, however, affect the matrices  $\mathbf{A}_{(k,l,m)}^{(i,j,k)}$ , and thus they need to be derived on a transformation-by-transformation basis. Furthermore, these submatrices become time-dependent and need to be recomputed at each timestep. For an arbitrary  $3 \times 3$  transformation with nine matrix elements, the analytical computation and hand-implementation of these matrices is error-prone. To remedy this, a metaprogramming scheme was developed. Mathematica was used to generate 243 C++ functions capable of computing the the matrix elements of the 27  $\mathbf{A}_{(k,l,m)}^{(i,j,k)}$  submatrices in terms of the quantities  $T_{ij}$  and  $T_{ij}^{-1}$ . Python was then used to auto-generate C++ code that populates the submatrices  $\mathbf{A}_{(k,l,m)}^{(i,j,k)}$  by calling the Mathematica-generated C++ functions. In this way, the multigrid system is automatically generated at each timestep and new simulation conditions can be immediately constructed by providing the matrix  $\mathbf{T}(t)$  as a  $3 \times 3$  matrix class implemented in C++.

### 3. Numerical convergence tests

In this section, convergence tests are provided for the coordinate transformation method. The work presented here is an extension of that in part I. The same staggered grid, domain decomposition scheme, parallelization methods, ghost regions, and finite-difference stencils are used here. Further information on implementation-specific details is provided in part I [1].

In all simulations, a periodic domain in  $X$  and  $Y$  is considered,  $-L \leq X < L$ ,  $-L \leq Y < L$  with  $L = 1$  cm. We consider both periodic and non-periodic boundary conditions in  $Z$ , corresponding to domains  $Z \in [-\gamma L, \gamma L)$  and  $Z \in [-\gamma L, \gamma L]$ , respectively. Here,  $\gamma = \frac{1}{2}$  in all simulations. We measure time in terms of the natural unit  $t_s = L/c_s$  with  $c_s = \sqrt{\mu/\rho}$  the material shear wave speed. Boundary conditions in the nonperiodic case are given by

$$\mathbf{V}(X, Y, \pm\gamma L, t) = (0, 0, 0). \quad (27)$$

Elasticity and plasticity parameters are given by Table 1 in part I [1], with the time scale being given by  $t_s = 4.05$   $\mu$ s. The global three-dimensional grid has the same structure as in part I, with a grid spacing of  $h$  in each direction. The cell-cornered grid points are indexed according to  $i = 0, \dots, Q - 1$ ,  $j = 0, \dots, M - 1$  in the  $X$  and  $Y$  directions. In the  $Z$  direction, the grid points are indexed according to  $k = 0, \dots, N$  and  $k = 0, \dots, N - 1$  for nonperiodic and periodic boundary conditions, respectively. The cell-centered grid points run according to  $i = \frac{1}{2}, \frac{3}{2}, \dots, Q - \frac{1}{2}$ ,  $j = \frac{1}{2}, \frac{3}{2}, \dots, M - \frac{1}{2}$ , and  $k = \frac{1}{2}, \frac{3}{2}, \dots, M - \frac{1}{2}$ .  $\Sigma$  and  $\chi$  are stored at cell centers while  $\mathbf{V}$  is stored at cell corners. The additional grid points  $(i, j, k = N)$  in the  $Z$  direction in the nonperiodic case are ghost points used for enforcing the Dirichlet boundary conditions  $\mathbf{V} = 0$ .

The cell-centered grid points on the top boundary  $(i, j, N + \frac{1}{2})$  contain linearly interpolated  $\Sigma$  and  $\chi$  values to ensure that  $\Sigma$  and  $\chi$  remain free on the top boundary. In the periodic

case, the grid points  $(i, j, k = N)$  contain the velocity values  $\mathbf{V}_{(i,j,0)}$ , and the corresponding cell-centered grid points are used to hold the wrapped values of  $\Sigma_{(i,j,\frac{1}{2})}$  and  $\chi_{(i,j,\frac{1}{2})}$ . At the simulation boundaries in the  $X$  and  $Y$  directions, ghost points leaving the simulation domain are filled with values that wrap around, so that the ghost point corresponding to grid point  $(Q, j, k)$  is filled with the real values from grid point  $(0, j, k)$ . Similarly, values at points  $(i, M, k)$  are filled in using values from  $(i, 0, k)$ .

### 3.1. Qualitative comparison between transformed and non-transformed method

We now demonstrate the qualitative similarity of solutions computed with the transformed and the standard quasi-static methods in a physically equivalent situation. In the following section, this comparison is made quantitatively rigorous. To visualize the results three-dimensionally, we use the same custom opacity function as in part I,

$$O(\mathbf{x}) = \begin{cases} \left( \frac{\chi(\mathbf{x}) - \chi_{bg}}{\chi_{\infty} - \chi_{bg}} \right) & \text{if } \frac{\chi(\mathbf{x}) - \chi_{bg}}{\chi_{\infty} - \chi_{bg}} > \frac{1}{2}, \\ \exp \left( -a \left( \frac{\chi_{\infty} - \chi_{bg}}{\chi(\mathbf{x}) - \chi_{bg}} \right)^{\eta} \right) & \text{otherwise.} \end{cases} \quad (28)$$

By choice of  $a$  and  $\eta$ , the most physically important features in three-dimensional visualizations of the  $\chi$  field can be revealed.

To compare the transformed and non-transformed methods, a physically equivalent situation was constructed. Non-periodic conditions in the  $Z$ -direction were used in the transformed simulation, with Dirichlet boundary conditions  $\mathbf{V}(X, Y, \pm\gamma L) = (0, 0, 0)$ . A shear transformation  $\mathbf{T}(t)$  corresponding to

$$\mathbf{T} = \begin{pmatrix} 1 & 0 & \frac{U_b t}{\gamma L} \\ 0 & 1 & 0 \\ 0 & 0 & 1 \end{pmatrix} \quad (29)$$

was used.

Boundary conditions in the non-transformed simulation correspond to shearing between two parallel plates,  $\mathbf{v}(x, y, \pm\gamma L) = (U_b, 0, 0)$ . An initial linear velocity gradient was imposed in the non-transformed frame, so that

$$\mathbf{v}(\mathbf{x}, t = 0) = \left( \frac{U_b z}{\gamma L}, 0, 0 \right). \quad (30)$$

Equation 30 ensures equivalent initial conditions, and also prevents the introduction of large gradients in the deformation rate near the boundary. To create interesting dynamics, an initial condition in  $\chi$  corresponding to a helix oriented perpendicular to the direction of shear was considered. Mathematically, this is represented as

$$\begin{aligned} \delta_x &= \frac{x}{L} - \left( \frac{\cos \left( 6\pi \left( \frac{y}{L} + 1 \right) \right)}{8} - \frac{1}{16} \right), \\ \delta_z &= \frac{z}{L} - \left( \frac{\cos \left( 6\pi \left( \frac{y}{L} + 1 \right) \right)}{8} - \frac{1}{16} \right), \\ \chi(\mathbf{x}, t = 0) &= 600 \text{ K} + (200 \text{ K}) e^{-750(\delta_x^2 + \delta_z^2)}. \end{aligned} \quad (31)$$

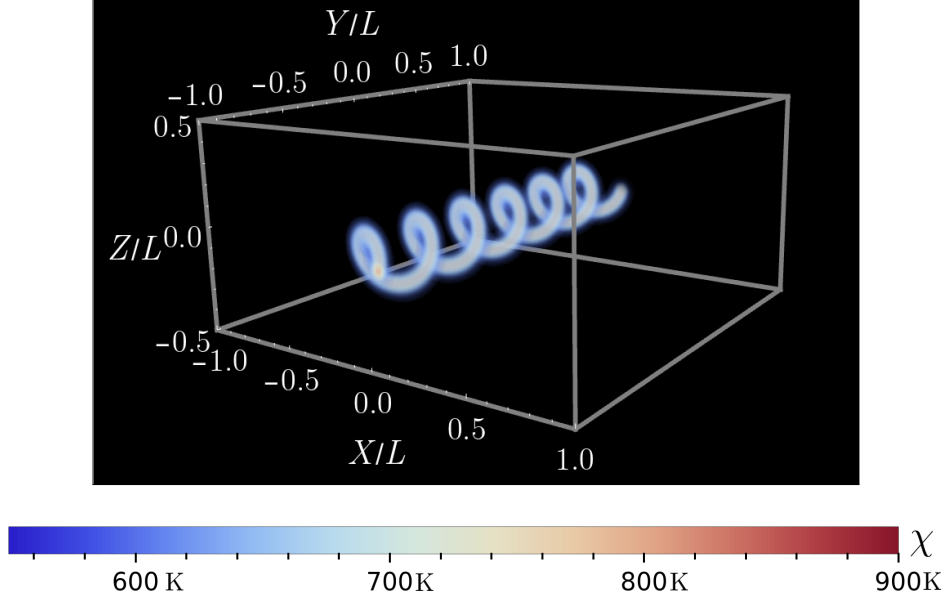


Figure 2: The initial configuration for the transformed to non-transformed comparison. Here,  $a = 0.35$  and  $\eta = 1.25$  in the opacity function.

Equation 31 is written in the non-transformed simulation, but the same initial conditions are used in the transformed simulation with the substitution  $\mathbf{x} \rightarrow \mathbf{X}$ . The configuration is visualized in Fig. 2.

The simulations were conducted on two grids of size  $256 \times 256 \times 128$ , with a quasi-static timestep  $\Delta t = 31.25t_s$ , and with a value of  $U_b = 10^{-7} \frac{L}{t_s}$ . Snapshots at three representative time points are shown in Fig. 3. In Fig. 3(a) at  $t = 2.88 \times 10^5 t_s$ , shear band nucleation has not begun, and there is an increase in the  $\chi$  field across the entire domain. At  $t = 4.02 \times 10^5$  in Fig. 3(b), shear bands have begun to nucleate along the top and bottom planes of the helices. At  $t = 6 \times 10^5 t_s$  in Fig. 3(c), the bands have grown sharper, stronger, and span the system. In all cases, the qualitative agreement is very good.

### 3.2. Quantitative comparison between the transformed and non-transformed methods

Having demonstrated the qualitative similarity between the solutions computed by the transformed and non-transformed methods, we now present a rigorous quantitative comparison. The same simulation geometry, boundary conditions, shear transformation, and initial conditions are used here as in Sec. 3.1. As in part I, a norm defined over simulation fields is introduced,

$$\|\mathbf{f}\|(t) = \sqrt{\frac{1}{8\gamma L^3} \int_{-\gamma L}^{\gamma L} dZ \int_{-L}^L dY \int_{-L}^L dX |\mathbf{f}(\mathbf{X}, t)|^2}, \quad (32)$$

where the integral in Eq. 32 runs over the entire simulation domain and is numerically computed using the trapezoid rule. The appearance of  $|\cdot|$  in Eq. 32 is interpreted as the two-norm for vectors, absolute value for scalars, and the Frobenius norm for matrices. With

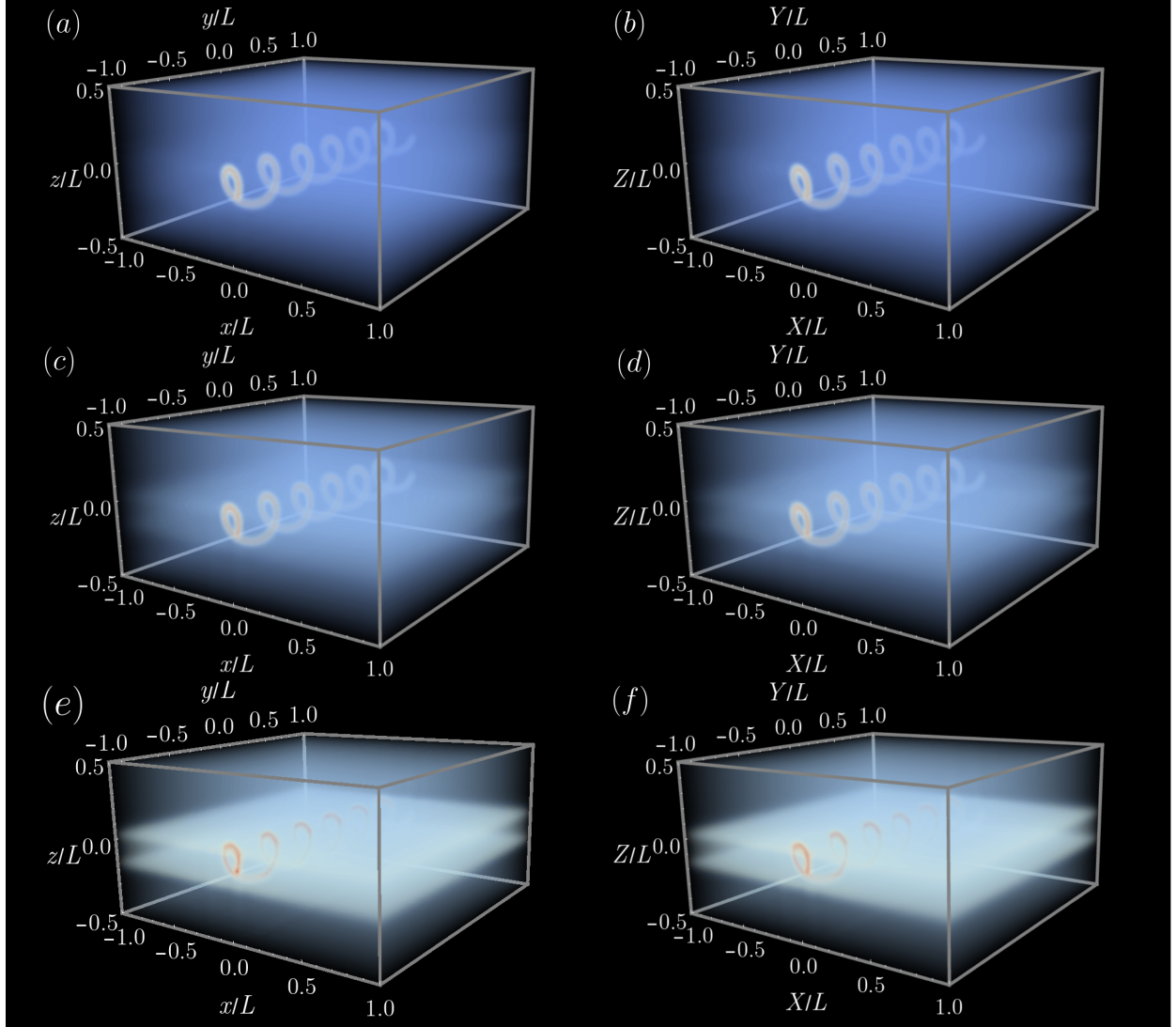


Figure 3: Snapshots of the effective temperature distribution  $\chi(\mathbf{x}, t)$  for the non-transformed (a,c,e) and transformed simulation (b,d,f). The color bar is the same as in Fig. 2. (a,b)  $t = 2.88 \times 10^5 t_s$ ,  $a = 0.7$ ,  $\eta = 1.25$ . (c,d)  $t = 4.02 \times 10^5 t_s$ ,  $a = 0.8$ ,  $\eta = 1.35$ . (e,f)  $t = 6 \times 10^5 t_s$ ,  $a = 0.9$ ,  $\eta = 1.5$ .

subscript NT denoting “non-transformed” and subscript T denoting “transformed”, Eq. 32 is applied to the quantities  $\mathbf{v}(\mathbf{X}, t)_{\text{NT}} - \mathbf{v}(\mathbf{X}, t)_{\text{T}}$ ,  $\boldsymbol{\sigma}(\mathbf{X}, t)_{\text{NT}} - \boldsymbol{\sigma}(\mathbf{X}, t)_{\text{T}}$  and  $\chi(\mathbf{X}, t)_{\text{NT}} - \chi(\mathbf{X}, t)_{\text{T}}$ . The *physical* field values are compared across the *reference* grid, a procedure that involves two subtleties.

In the transformed simulation, this comparison requires computing  $\boldsymbol{\sigma}$  from  $\boldsymbol{\Sigma}$  and  $\mathbf{v}$  from  $\mathbf{V}$  using Eqs. 13 and 10 respectively at all reference grid points. In the non-transformed simulation, it is necessary to compute the non-transformed field values at reference grid points. Because the reference grid maps to a sheared physical grid, these values may not be defined in the non-transformed simulation. We handle this via the following procedure. The non-transformed simulation grid point  $\mathbf{x}(\mathbf{X})$  corresponding to the reference grid point  $\mathbf{X}$  is first computed. If  $\mathbf{x}(\mathbf{X})$  does not lie on the non-transformed grid, adjacent grid points are linearly interpolated to compute an approximate field value at  $\mathbf{x}$ . This procedure incurs an  $\mathcal{O}(h^2)$  error, which is the same order of accuracy as the centered differences used for spatial discretization in the two methods. As the sizes of the simulation grids are increased, the discrepancy in solutions will decrease.

To ensure that issues with temporal discretization do not affect the comparison, it is also necessary to scale the quasi-static timestep as the grid size is decreased. Because the spatial order of accuracy is  $\mathcal{O}(h^2)$ , we keep the ratio  $\Delta t/h^2$  fixed across all simulations. Comparisons were performed across grids of size  $N \times N \times \frac{N}{2}$  with  $N = 64, 96, 128, 160, 192$ , and  $256$ . Respectively, these correspond to grid spacings  $L/32, L/48, L/64, L/80, L/96$ , and  $L/128$ . The quasi-static timestep was chosen to be  $\Delta t = 500t_s$  for the coarsest simulation, leading to quasi-static timesteps  $\Delta t = 222.14, 125, 80, 55.55$ , and  $31.25$  respectively. The diffusion length scale in the effective temperature equation is taken to be zero in all simulations for the purpose of the comparison.

The results for the quantitative comparisons are shown in Fig. 4. In Fig. 4(a), the three  $L_2$  norm curves are plotted together for a value of  $N = 256$ , where each curve is normalized by a representative value in order to plot on a comparable dimensionless scale. The effective temperature norm increases rapidly early on in the simulation, but then saturates around  $10^{-4}$ . The  $\boldsymbol{\sigma}$  norm stays around machine precision until the onset of plasticity, when it rapidly increases and then saturates around  $10^{-3}$ . Similarly, the  $\mathbf{v}$  norm stays below  $10^{-13}$  until the onset of plasticity, when it rapidly increases and then saturates around  $10^{-4}$ . The agreement up to machine precision prior to the onset of plasticity is expected, and validates the accuracy of the derivation of the equations in the reference frame.

In Fig. 4(b), the effective temperature norm curves are shown for all values of  $N$ . Here, there is a steady increase in the discrepancy before the onset of plasticity due to advection across the grid. After plasticity is activated around  $t = 1.2 \times 10^5 t_s$ , there is a period of saturation in all curves, followed by a period of increase beginning around  $t \approx 3 \times 10^5 t_s$ , where some simulation curves cross and end at roughly equal values. For the majority of the simulation, the expected decrease in discrepancy with smaller grid spacing is observed.

In Fig. 4(c), the velocity norm curves are shown as a function of time for all discretization levels. In all cases, the difference between the simulation methods is on the order of machine precision until the onset of plasticity, when there is a sharp and immediate jump. The size of

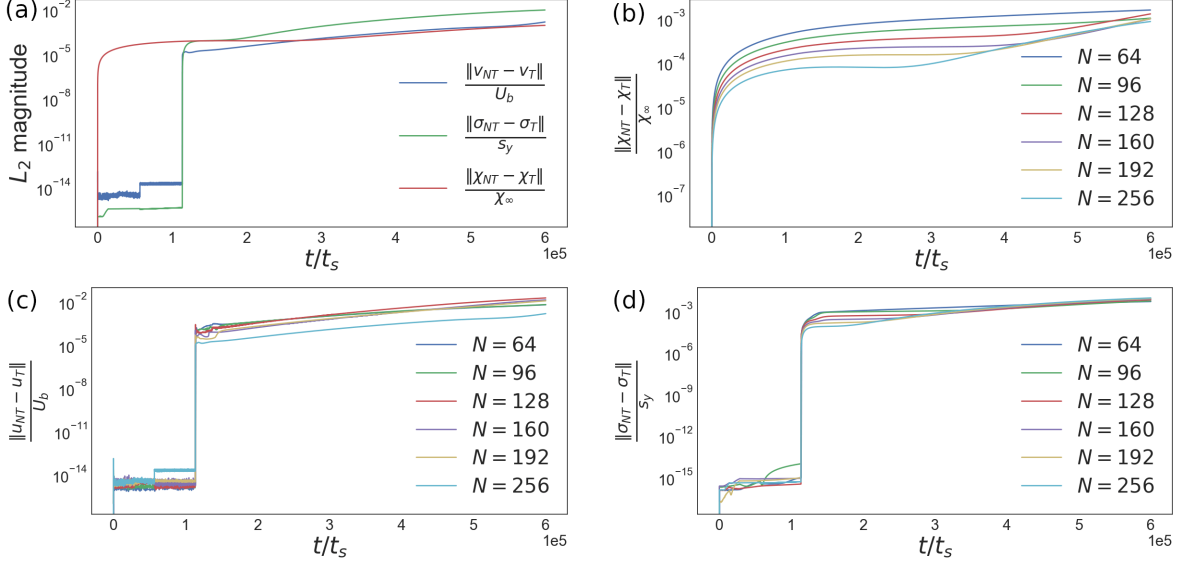


Figure 4:  $L_2$  norm of the  $\chi$ ,  $\mathbf{v}$ , and  $\boldsymbol{\sigma}$  simulation field differences between the transformed and non-transformed methods computed using Eq. 32 in a simple shear simulation. (a) A comparison of the three different field norms on a grid of size  $256 \times 256 \times 128$ . (b), (c), (d) The velocity, effective temperature, and stress norm differences respectively for varying levels of discretization  $N = N_x = N_y = 2N_z$ .

the jump decreases with the discretization level as expected.

In Fig. 4(d), the stress norm curves are shown. These curves display a combination of the trends in the velocity and effective temperature plots. Before the onset of plasticity, the error in all simulations is very low, on the order of machine precision. After the onset of plasticity, there is a sharp jump in all simulations, and the size of the jump decreases with more grid points. Past around  $t \approx 2 \times 10^5 t_s$ , the curves begin to cross, all ending at roughly equivalent values.

## 4. Numerical examples

### 4.1. Simple shear and the effect of Lees–Edwards boundary conditions

As a first example application of the transformation method, we consider connecting a continuum-scale model to discrete molecular dynamics simulation. A significant difference between continuum simulation and molecular dynamics is in the boundary conditions. Molecular dynamics simulations commonly employ Lees–Edwards boundary conditions, where periodic copies of the system are placed above and below with a horizontal velocity. Continuum-scale boundary conditions usually prescribe a shear velocity on the top and bottom boundaries to achieve the same effect.

Lees–Edwards boundary conditions can be implemented in the continuum through the use of the coordinate transformation methodology presented here, by combining a shear transformation  $\mathbf{T}(t)$  as in Eq. 19 with periodicity in the  $Z$  direction. In the following

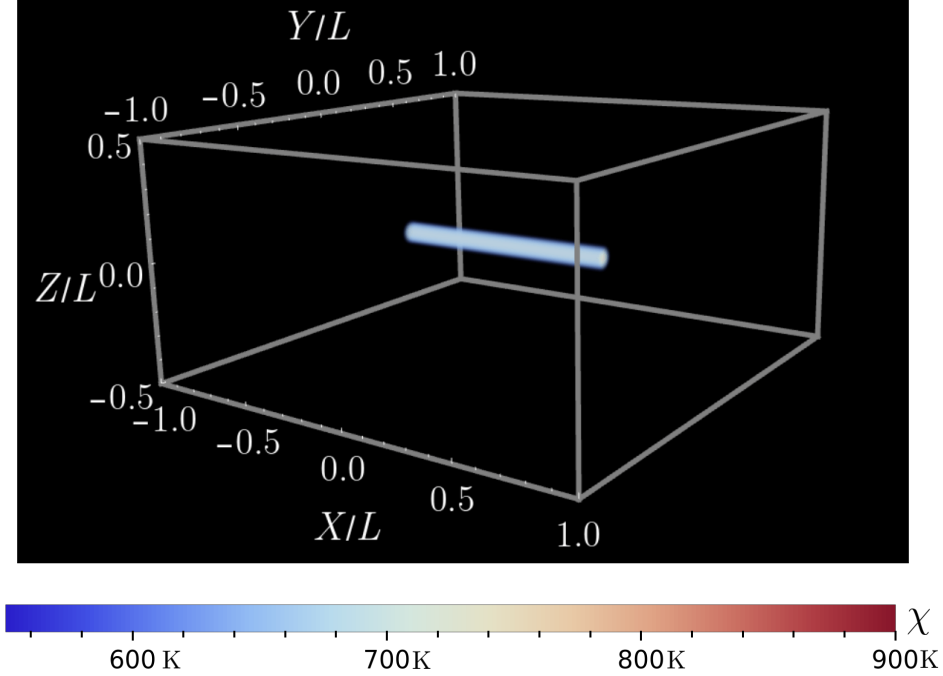


Figure 5: The initial conditions for the cylindrical numerical experiments.

sections, we present several numerical examples using Lees–Edwards and nonperiodic boundary conditions. Particular attention is paid to differences in shear banding dynamics produced by these two choices of boundary conditions.

#### 4.1.1. Cylindrical inclusion

We first consider an initial condition corresponding to a cylindrical defect in the material. The effective temperature field is elevated along a cylinder of finite length oriented along the direction of shear. The initial condition in the effective temperature field is given by

$$\chi(\mathbf{X}, t = 0) = 550 \text{ K} + (200 \text{ K}) e^{-500(Z^2 + Y^2)} \quad (33)$$

for  $x > a_X/2$  and  $x < b_X/2$ , and 550 K otherwise. The initial condition is shown in Fig. 5.

Results for Lees–Edwards and nonperiodic boundary conditions are shown in Fig. 6, on the right and left respectively. The shear banding dynamics in this case are simple, and are similar to the central defect simulations considered in part I. In this case, the dynamics are virtually identical for the Lees–Edwards and nonperiodic boundary conditions.

At  $t = 5 \times 10^4 t_s$  in Fig. 6 (a/b), nucleation of the shear band has begun, and there is some spreading in the  $\chi$  field visible at the caps of the cylinder. By  $t = 10^5 t_s$ , a prominent system-spanning shear band has formed, as displayed in Fig. 6 (c/d). In Fig. 6 (e/f), the shear band continues to grow stronger and thicker.

#### 4.1.2. A randomly fluctuating effective temperature field

We now consider a randomly distributed initial condition in the effective temperature field  $\chi(\mathbf{X}, t = 0)$ . The same procedure used in part I is employed here [1]. For computational

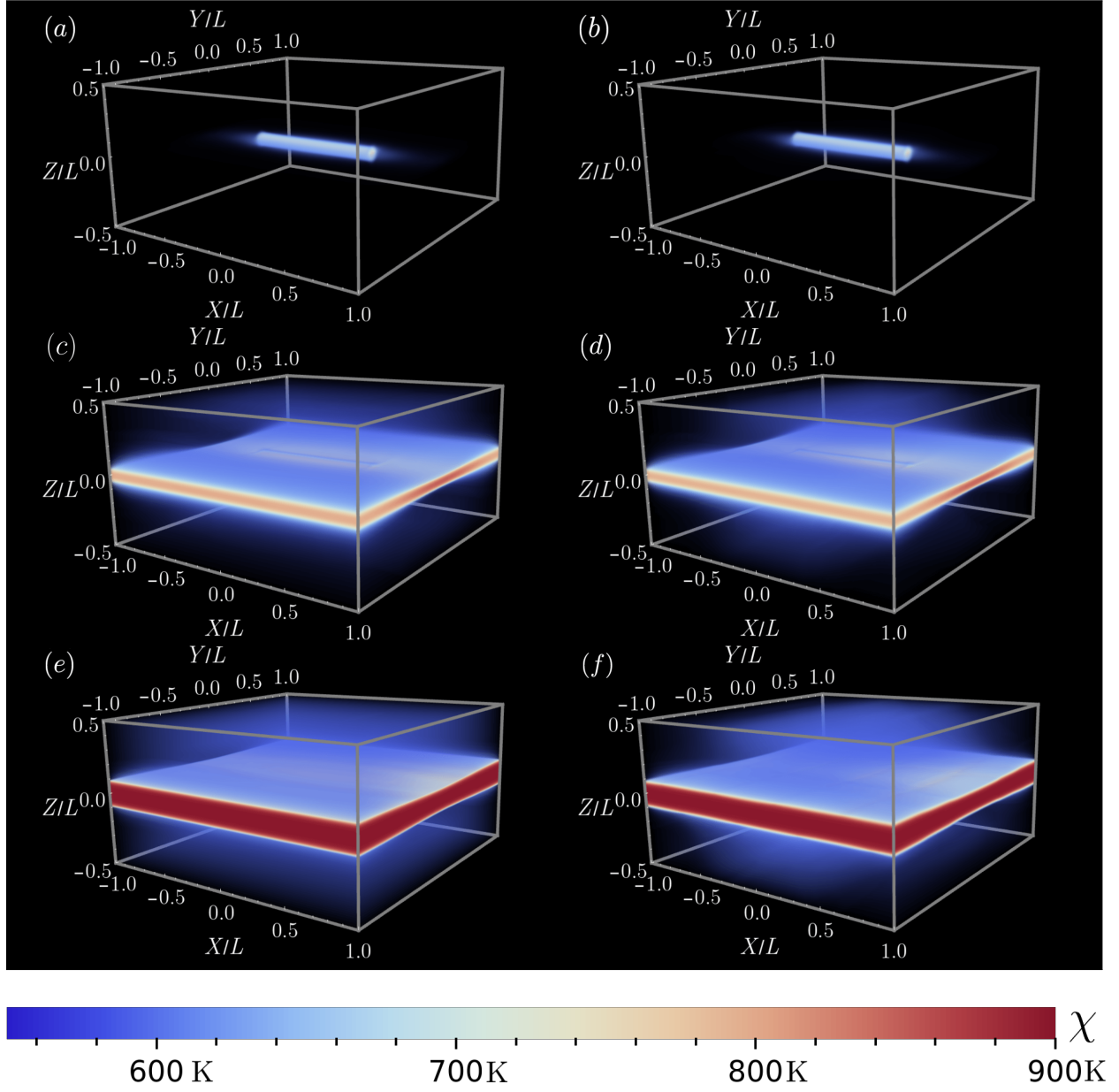


Figure 6: Snapshots of the effective temperature distribution  $\chi(\mathbf{X}, t)$  for a quasi-static simulation. Simple shear deformation is imposed via a domain transformation. The initial condition in  $\chi$  corresponds to a cylindrical inclusion as described in Sec. 4.1.1 and shown in Fig. 5. On the left, clamped boundary conditions in  $Z$  are used, while on the right, Lees-Edwards boundary conditions are used.  $a = 0.35$  and  $\eta = 1.25$  in all subfigures. (a/b)  $t = 5 \times 10^4 t_s$  (c/d)  $t = 10^5 t_s$  (d/e)  $t = 4 \times 10^5 t_s$ .

feasibility, a cutoff length of  $5l$  is used, so that the Gaussian kernel is considered to be zero past this point. In the following studies, a value of  $l = 5h$  is used.

Simulations were performed for mean values  $\mu_\chi = 450$  K, 500 K, 525 K, 550 K, 575 K, 600 K with a fixed value of  $\sigma_\chi = 15$  K for nonperiodic and Lees–Edwards boundary conditions. The diffusion length scale was set to  $l = \frac{3}{2}h$ , and the quasi-static timestep was set to  $\Delta t = 200t_s$ . The simulations were all conducted with a value of  $\gamma = \frac{1}{2}$  on a  $256 \times 256 \times 128$  cell grid to a final value of  $t = 1.5 \times 10^6 t_s$ . To induce shear banding, a shear transformation of the form Eq. 19 with a value of  $U_b = 10^{-7}L/t_s$  was imposed on the domain.

The results for this sequence of simulations in the case of nonperiodic boundary conditions are shown in Figs. 7–9. Each figure corresponds to a single snapshot in time, and the mean increases from left to right. The value of  $\chi_{bg}$  used in the opacity function in each case is given by  $\mu_\chi - 25$ . The same color bar is used across all figures, and is shown in Fig. 7, which displays the initial conditions in the effective temperature field. At  $t = 0$ , all simulations look essentially the same. The realization of the noise in each configuration is identical, and each pane is obtained from the previous by a constant shift in  $\chi$ .

By  $t = 4 \times 10^5 t_s$  in Fig. 8, the simulations with the two lowest values of  $\mu_\chi$  exhibit clear shear bands with curvature in both the  $X$  and  $Y$  directions. The single band in the center of the simulation is also apparent in Fig. 8(c), but it is significantly weaker and there is less curvature in both directions.

Fig. 9 ( $t = 10^6 t_s$ ) now displays clear shear banding across all values of  $\mu_\chi$ , and makes clear the dependence of shear banding structure on  $\mu_\chi$ . There is one primary band in Fig. 9(b), with a split near around  $\frac{X}{L} \approx -0.5$  not present in Fig. 9(a). Fig. 9(c) displays a split in its top band near  $\frac{Z}{L} \approx 0$ , an additional prominent band below it, and a very weak band mid-formation near the top of the simulation domain. Fig. 9(d) demonstrates a strengthening in the weakest band highest in  $Z/L$  relative to Fig. 9(c). Fig. 9(e) shows three clear, thin bands, while Fig. 9(f) shows the same three, plus an additional two near the top and bottom boundaries.

Taken together, Figs. 7–9 provide qualitative insight into how macroscopic shear banding dynamics and structure reflect the underlying effective temperature distribution. In a simulation with small mean, there are few regions susceptible shear band nucleation, most clearly displayed in the formation of only a single band in the two lowest mean simulations. These nucleation points must connect to form a band, as indicated by the curvature seen in bands formed at low  $\mu_\chi$ . As  $\mu_\chi$  is increased, additional regions of high enough  $\chi$  exist for band nucleation, curvature decreases, and the number of bands increases. This first presents itself, as seen in Figs. 7(b)–9(b), as an existing band splitting into two (or a gap in a thicker band). The gap in the split grows with  $\mu_\chi$ , as seen in Figs. 7(c)–9(c) and Figs. 7(d)–9(d), until it eventually breaks off into its own band. With high enough  $\mu_\chi$  as in Figs. 7(e)–9(e) and Figs. 7(f)–9(f), the background field is high enough that bands can nucleate in many different locations without curvature.

The results for an identical sequence of simulations in the case of Lees–Edwards boundary conditions are displayed in Figs. 10–12. The same color bar as before is used in all figures, and is shown in Fig. 7. The initial conditions are displayed in Fig. 10, which differ from those

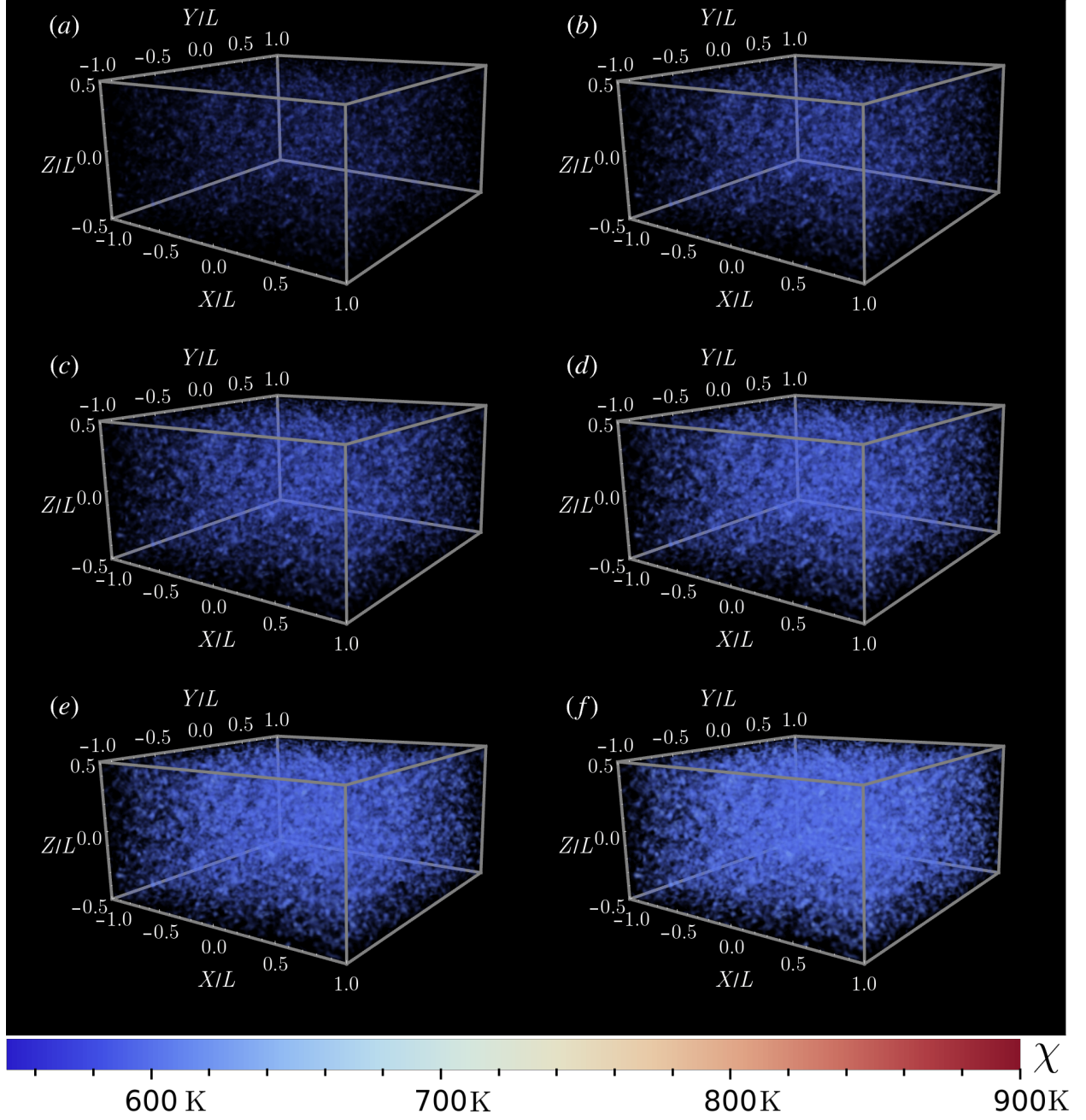


Figure 7: Snapshots of the effective temperature field at  $t = 0t_s$ . For all plots, a value of  $a = 0.25$  and  $\eta = 1.3$  is used in the opacity function. Figures (a)–(f) have  $\mu_\chi = 450$  K, 500 K, 525 K, 550 K, 575 K, and 600 K respectively.

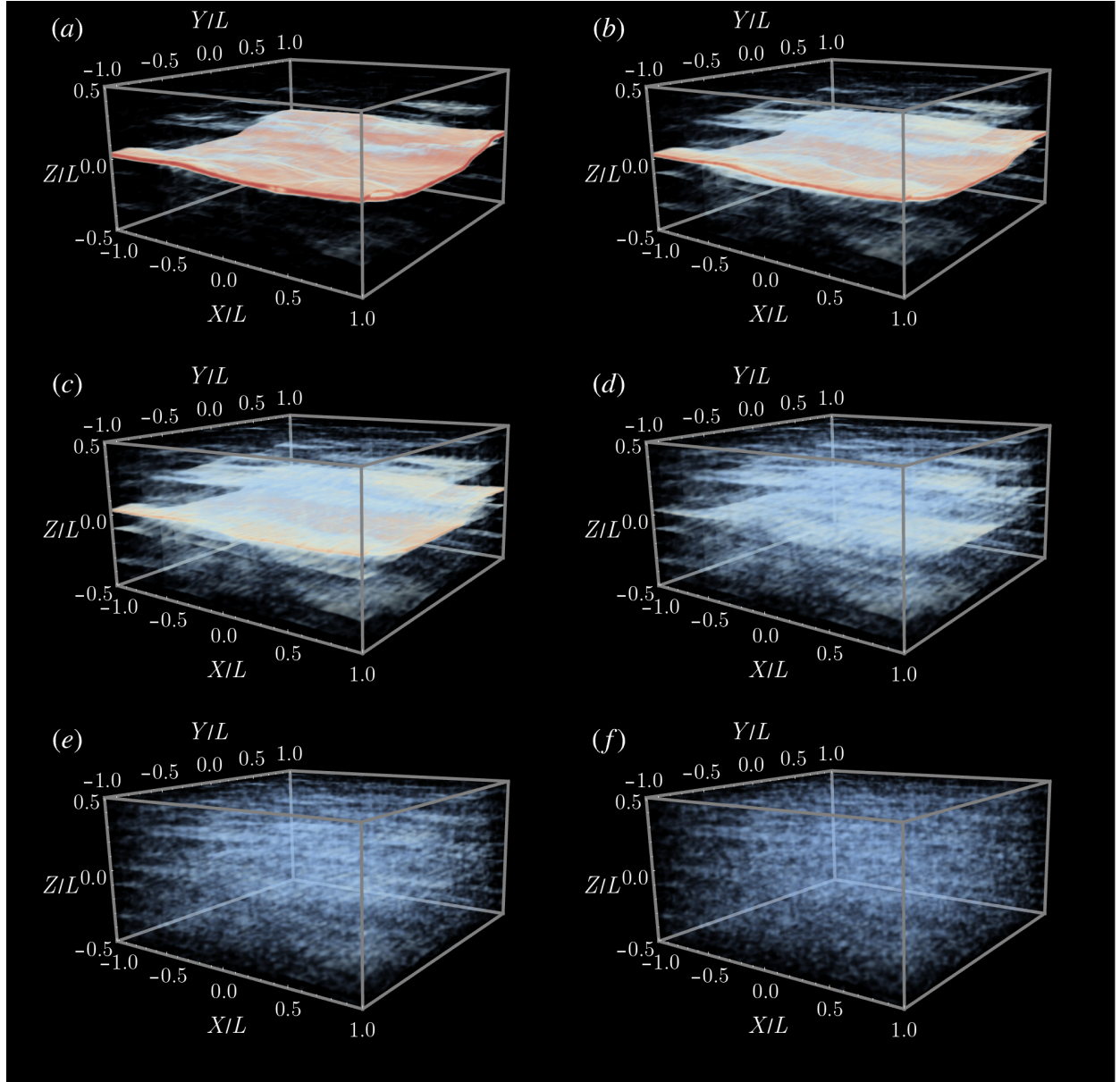


Figure 8: Snapshots of the effective temperature field at  $t = 4 \times 10^5 t_s$ . For all plots, a value of  $a = 0.45$  and  $\eta = 1.75$  is used in the opacity function. Figures (a)–(f) have  $\mu_\chi = 450$  K, 500 K, 525 K, 550 K, 575 K, and 600 K respectively. The color scheme is the same as given by the color bar in Fig. 7.

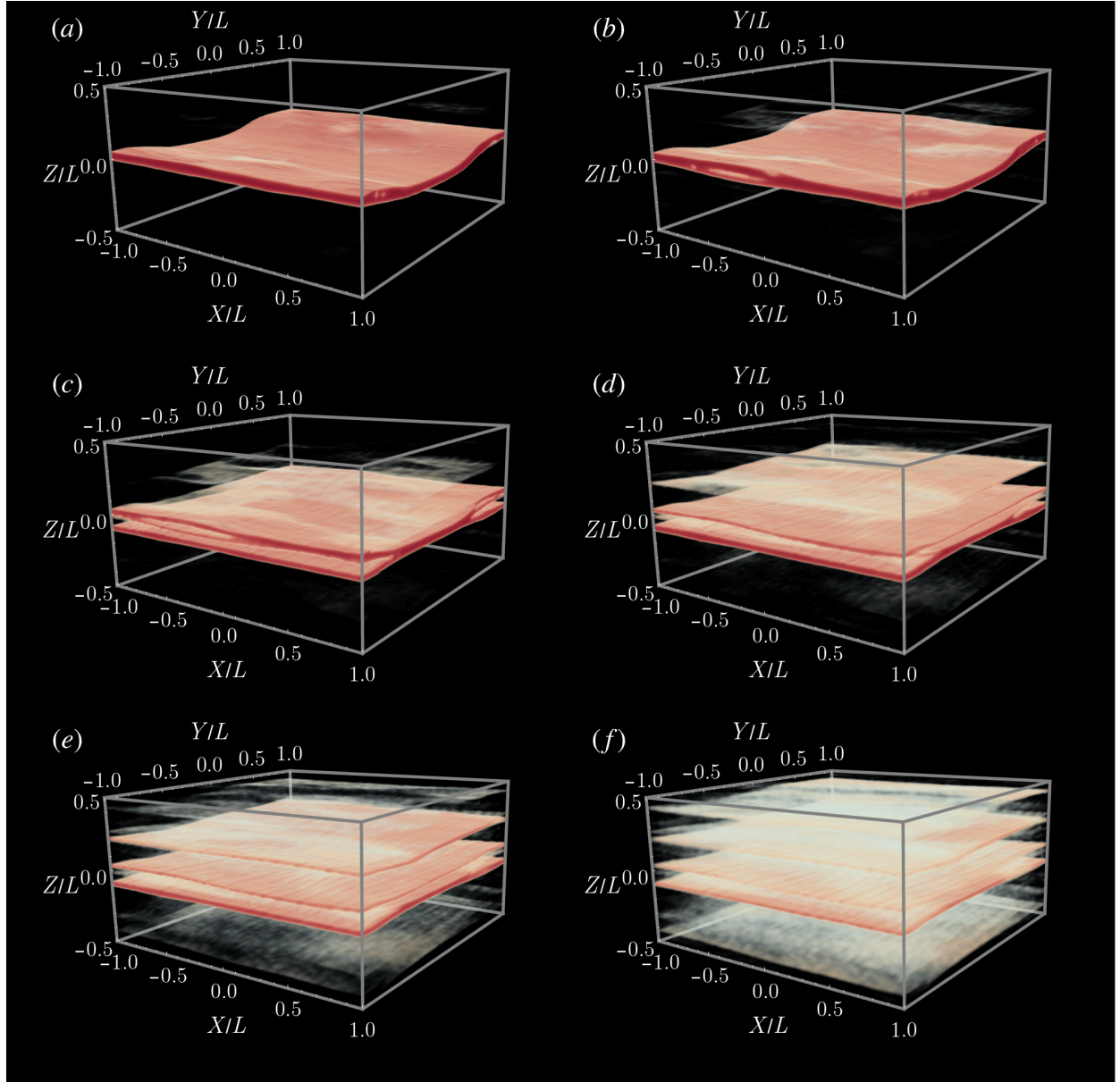


Figure 9: Snapshots of the effective temperature field at  $t = 10^6 t_s$ . For all plots, a value of  $a = 0.75$  and  $\eta = 2$  is used in the opacity function. Figures (a)–(f) have  $\mu_\chi = 450$  K, 500 K, 525 K, 550 K, 575 K, and 600 K respectively. The color scheme is the same as given by the color bar in Fig. 7.

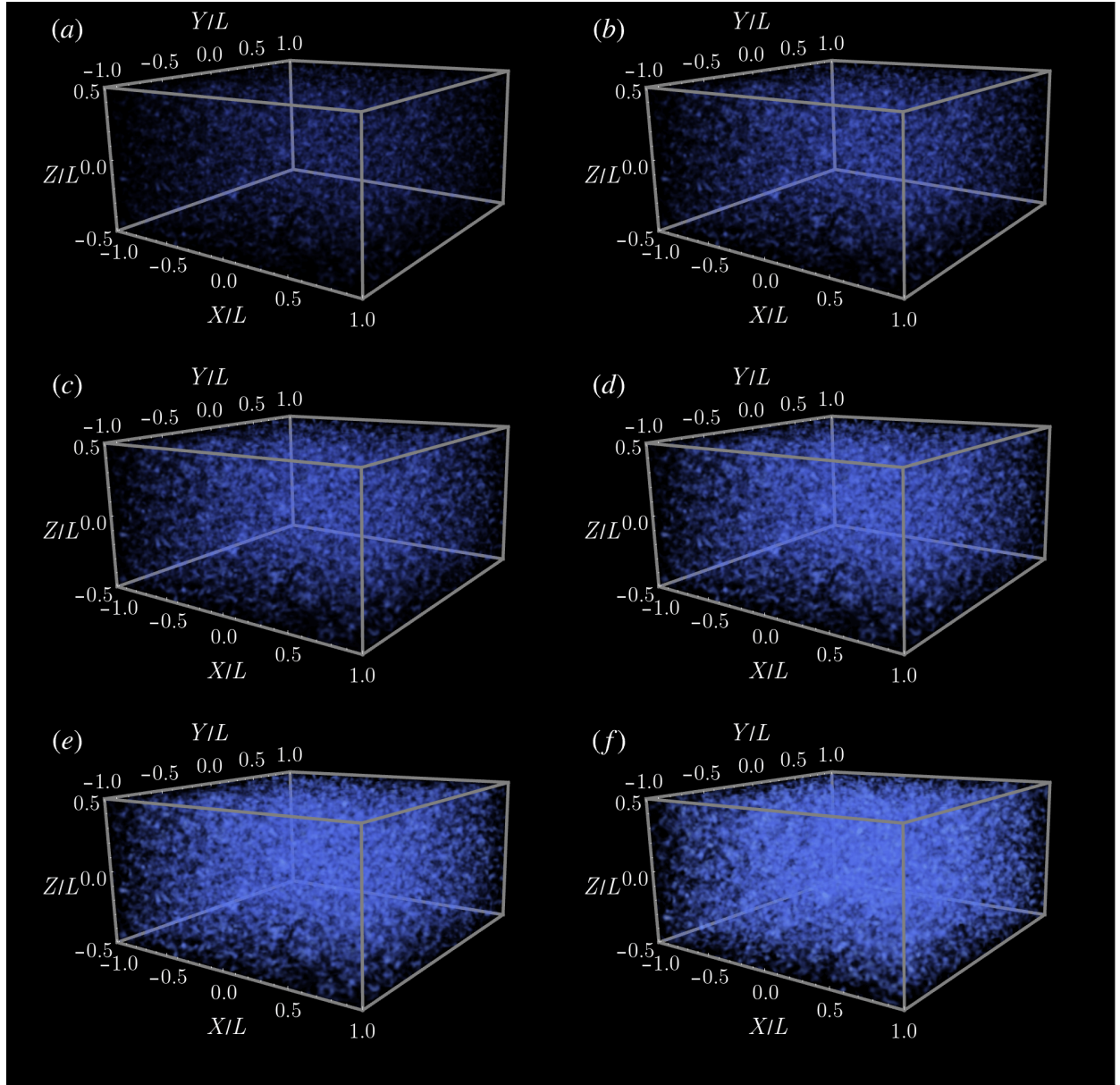


Figure 10: Snapshots of the effective temperature field at  $t = 0t_s$ . For all plots, a value of  $a = 0.25$  and  $\eta = 1.3$  is used in the opacity function. Figures (a)–(f) have  $\mu_\chi = 450$  K, 500 K, 525 K, 550 K, 575 K, and 600 K respectively. These simulations use Lees–Edwards boundary conditions by enforcing periodicity in the  $X$ ,  $Y$ , and  $Z$  directions. The color bar is the same as in Fig. 7

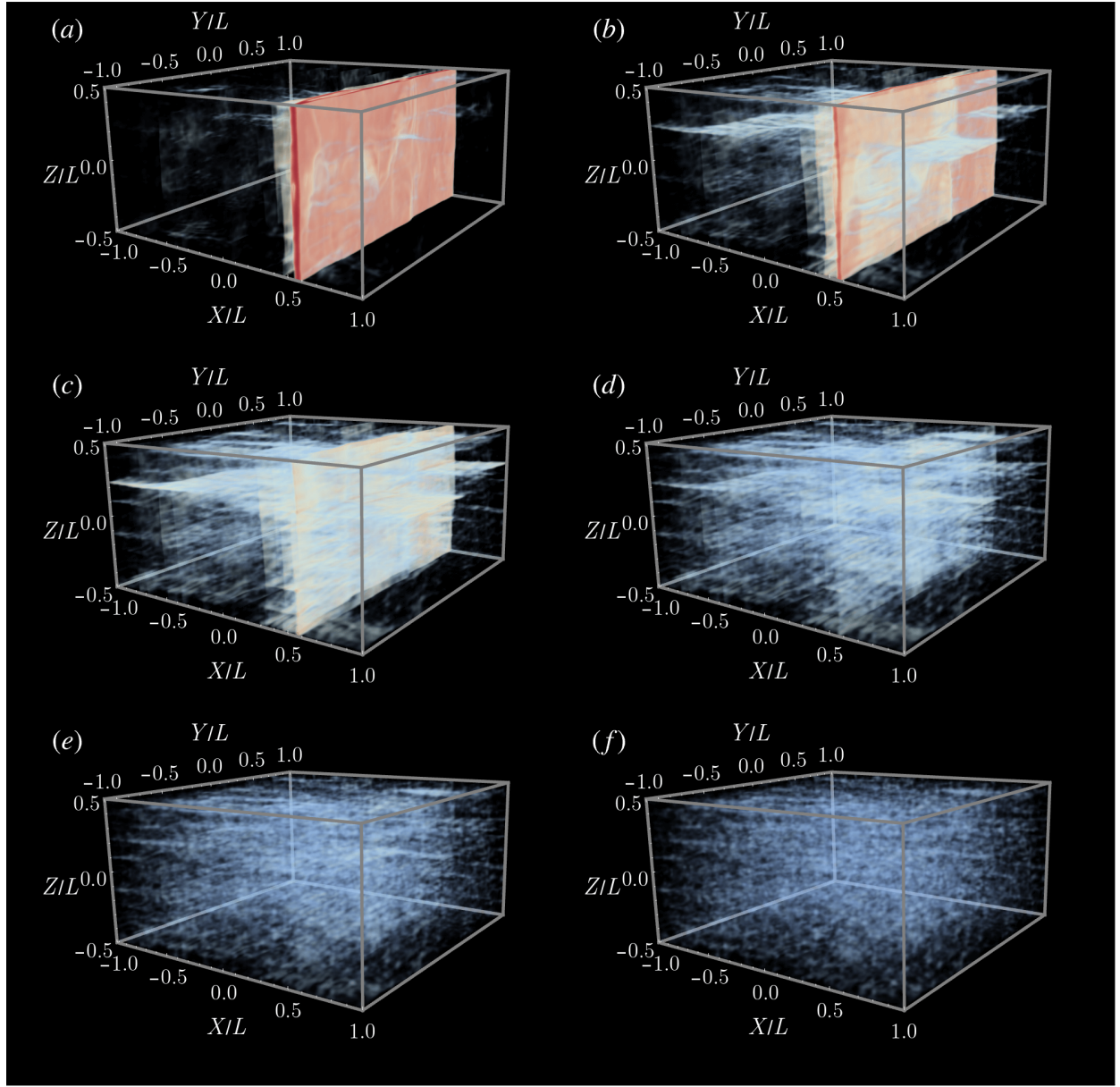


Figure 11: Snapshots of the effective temperature field at  $t = 4 \times 10^5 t_s$ . For all plots, a value of  $a = 0.45$  and  $\eta = 1.75$  is used in the opacity function. Figures (a)–(f) have  $\mu_\chi = 450$  K, 500 K, 525 K, 550 K, 575 K, and 600 K respectively. These simulations use Lees–Edwards boundary conditions by enforcing periodicity in the  $X$ ,  $Y$ , and  $Z$  directions. The color scheme is the same as given by the color bar in Fig. 7.

in Fig. 7, as the convolution used to generate the initial distribution now wraps around over the boundary in  $Z$ .

By  $t = 4 \times 10^5 t_s$  in Fig. 11(a), a single vertical shear band has formed which splits and recombines along  $Y$ . This single vertical band is also visible in Fig. 11(b), along with another vertical band nucleating nearby, and a third horizontal shear band forming perpendicular to the two vertical bands. Vertical shear bands do not typically form in continuum simulations with nonperiodic boundary conditions in  $Z$ , but are frequently seen in MD simulations [2, 41], indicating that the orientation of shear bands could be strongly related to the specific boundary conditions used. In Fig. 11(c), the same two vertical bands are visible in an earlier stage of development. The same horizontal band is also seen forming in the background.

Figure 12 shows the results for  $t = 10^6 t_s$ . Figure 12(a) displays the development of a horizontal band perpendicular to the vertical band. Fig. 12(b) shows two new curved horizontal bands. To the right of the rightmost vertical band is a diagonal strip of elevated  $\chi$  connecting the upper and lower horizontal bands. Figure 12(c) shows similar features, with only one weaker vertical band. The diagonal connecting band in this case originates at the vertical band and continues to the leftmost edge of the simulation. In Fig. 12(d), the second vertical band has disappeared, and an additional horizontal band has formed near the top of the simulation. Fig. 12(e) is similar to Fig. 12(d) with less vertical features. Figure 12(f) displays nearly identical features to Fig. 12(e), with more horizontal features in the lower portion.

Figure 12 clearly demonstrates the effect of increasing  $\mu_\chi$  with periodic boundary conditions. In the simulations with lower  $\mu_\chi$ , nucleation of vertical shear bands is more likely, and curved horizontal bands develop later in the simulation than vertical bands. As  $\mu_\chi$  is increased, the vertical bands begin to disappear. As in the nonperiodic case, the curvature in the horizontal bands decreases with  $\mu_\chi$ . As  $\mu_\chi$  is increased further, the vertical bands disappear altogether. In this regime, increasing  $\mu_\chi$  increases the number of horizontal bands, and the qualitative agreement with the nonperiodic results is good. These results suggest that, for higher  $\mu_\chi$ , the effect of periodicity in the  $Z$  direction is less significant. Furthermore, given the prevalence of vertical band formation in molecular dynamics simulations, the disappearance of vertical bands for higher  $\mu_\chi$  suggests that typical molecular dynamics configurations may correspond to a distribution in  $\chi$  with a lower value of  $\mu_\chi$ .

#### 4.2. Pure shear

As a second example transformation, we now consider pure shear deformation. In metallic glasses, experimental evidence indicates that pure shear is the primary failure mode under compressive stress, and several recent experiments have been conducted probing BMGs under pure shear conditions [42, 43, 44, 45]. Pure shear is particularly interesting due to the simplicity of its implementation in the transformation methodology. To simulate pure shear on a physical grid, it would be necessary to impose traction boundary conditions on the top, bottom, and sides, which poses computational difficulties. Within the transformation

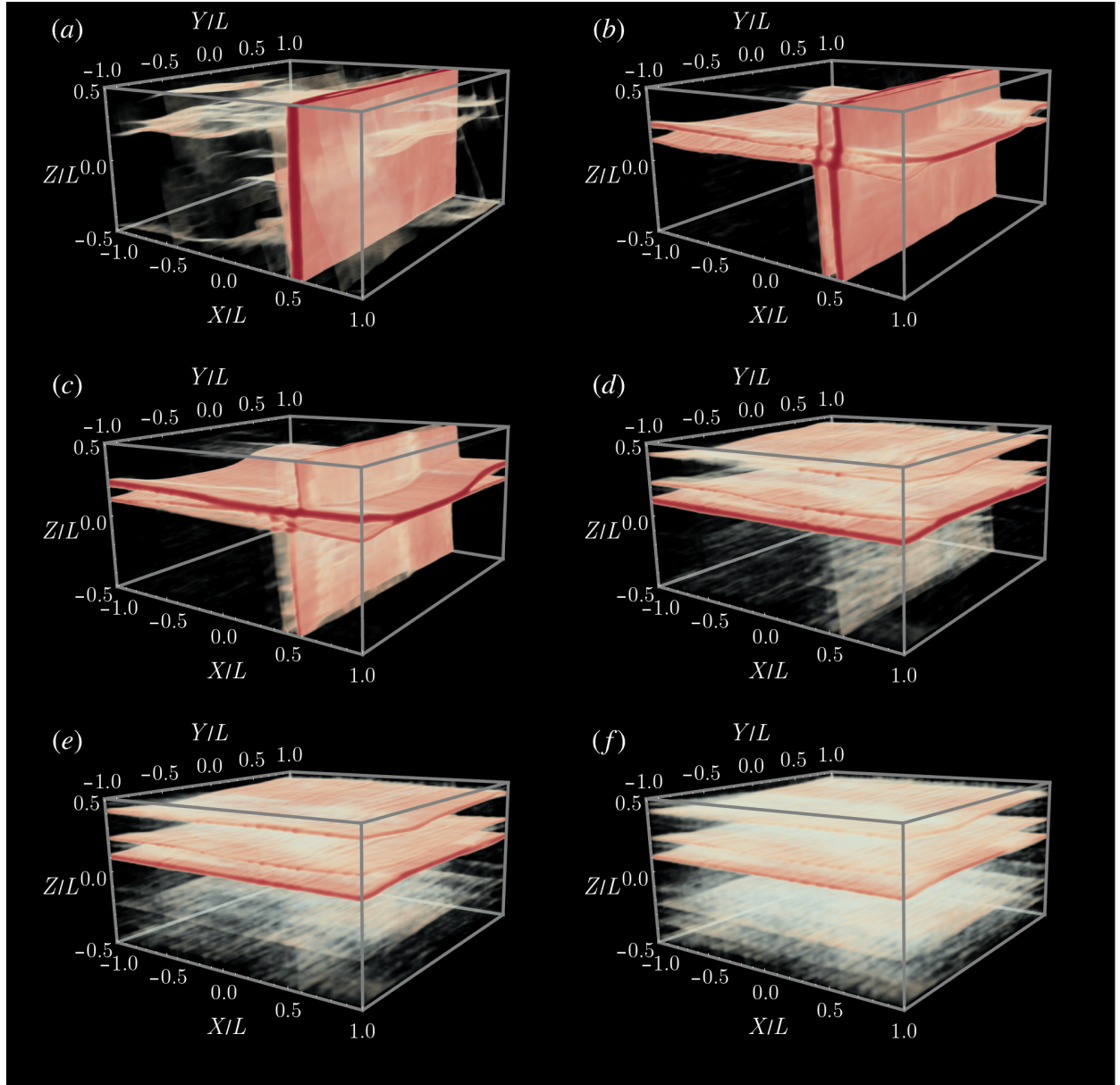


Figure 12: Snapshots of the effective temperature field at  $t = 10^6 t_s$ . For all plots, a value of  $a = 0.75$  and  $\eta = 2$  is used in the opacity function. Figures (a)–(f) have  $\mu_\chi = 450$  K, 500 K, 525 K, 550 K, 575 K, and 600 K respectively. These simulations use Lees–Edwards boundary conditions by enforcing periodicity in the  $X$ ,  $Y$ , and  $Z$  directions. The color scheme is the same as given by the color bar in Fig. 7.

framework, pure shear can be readily implemented using the following transformation

$$\mathbf{T}(t) = \begin{pmatrix} A(t) & 0 & 0 \\ 0 & 1 & 0 \\ 0 & 0 & \frac{1}{A(t)} \end{pmatrix}. \quad (34)$$

$A(t)$  can be chosen as any monotonically increasing function of time. In the following studies, we choose  $A(t) = e^{\xi t}$ , where  $\xi$  is a simulation parameter that sets the rate of extension and compression of the  $x$  and  $z$  axes respectively.

#### 4.2.1. Gaussian defects

To gain some physical intuition about shear banding dynamics with pure shear boundary conditions, we first consider an example initial condition in  $\chi$  corresponding to localized defects in the material. It is expected that diagonal shear bands will nucleate outwards from the imperfections. We first define the quantities

$$\begin{aligned} \mathbf{X}_1 &= (-0.3, -0.3, 0.2), \\ \mathbf{X}_2 &= (0.3, 0.3, -0.2), \\ \mathbf{X}_3 &= (-0.1, -0.1, 0.1), \\ \mathbf{X}_4 &= (0.1, 0.1, -0.1), \\ \mathbf{X}_5 &= (0, 0, 0), \\ \delta_1 &= \delta_2 = \delta_5 = 200, \\ \delta_3 &= \delta_4 = 150, \end{aligned}$$

and then take the initial condition in  $\chi$  to be

$$\chi(\mathbf{X}, t = 0) = 550 \text{ K} + (200 \text{ K}) \sum_{i=1}^5 e^{-\delta_i \|\mathbf{X} - \mathbf{X}_i\|^2}. \quad (35)$$

Simulations were performed with periodic and nonperiodic boundary conditions in  $Z$  on grids of size  $256 \times 256 \times 128$  with  $\gamma = \frac{1}{2}$ . The  $X$  and  $Y$  dimensions use periodic boundary conditions in both cases. The diffusion length scale was set to  $l = 3h$  and the quasi-static timestep was  $\Delta t = 200t_s$ .  $\xi$  in Eq. 34 was set to be  $4/t_f$  with  $t_f = 4 \times 10^5 t_s$  the simulation duration, so that  $A(t_f) = e^{1/4} \approx 1.284$ .

Results for Lees–Edwards and nonperiodic boundary conditions are shown in Figs. 13 and 14 respectively. The initial conditions are shown in Figs. 13(a) and 14(a). In both Figs. 13(b) and 14(b) at  $t = 5 \times 10^4 t_s$ , some spreading in the  $\chi$  field is seen near the defects. Shortly thereafter, the dynamics in the nonperiodic and periodic cases begin to differ dramatically.

At  $t = 8 \times 10^4 t_s$  in Fig. 13(c), three diagonal bands are seen connecting through the defects. The bands become more pronounced at  $t = 10^5 t_s$  in Fig 13(d). This continues into  $t = 2 \times 10^5 t_s$  in Fig. 13(e), along with the addition of diagonal bands perpendicular to the original bands. Both bands continue to grow larger and stronger by  $t = 4t \times 10^5 t_s$  in Fig. 13(f).

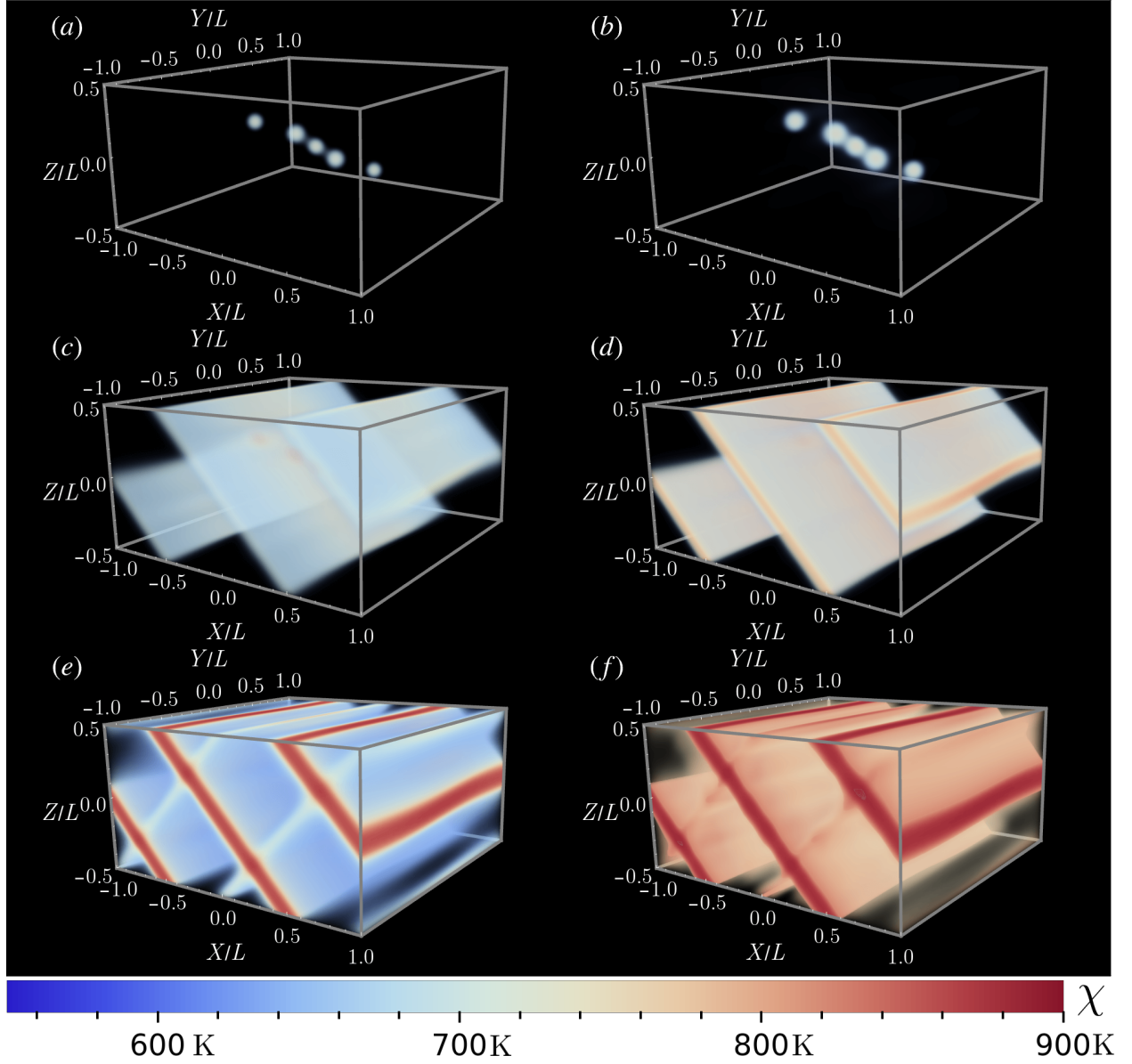


Figure 13: Snapshots of the effective temperature distribution  $\chi(\mathbf{X}, t)$  for a quasi-static simulation. Pure shear deformation is imposed via a domain transformation with an initial condition corresponding to a sequence of blips of elevated  $\chi$  lying roughly along the superdiagonal of the simulation domain. This simulation uses Lees–Edwards boundary conditions and is periodic in all three directions. (a)  $t = 0t_s$ ,  $a = 0.75$ ,  $\eta = 1.2$ . (b)  $t = 5 \times 10^4 t_s$ ,  $a = 0.75$ ,  $\eta = 1.2$ . (c)  $t = 8 \times 10^4 t_s$ ,  $a = 0.75$ ,  $\eta = 1.25$ . (d)  $t = 10^5 t_s$ ,  $a = 0.75$ ,  $\eta = 1.25$ . (e)  $t = 2 \times 10^5 t_s$ ,  $a = 0.4$ ,  $\eta = 1.6$ . (f)  $t = 4 \times 10^5 t_s$ ,  $a = 1.1$ ,  $\eta = 2.45$ .

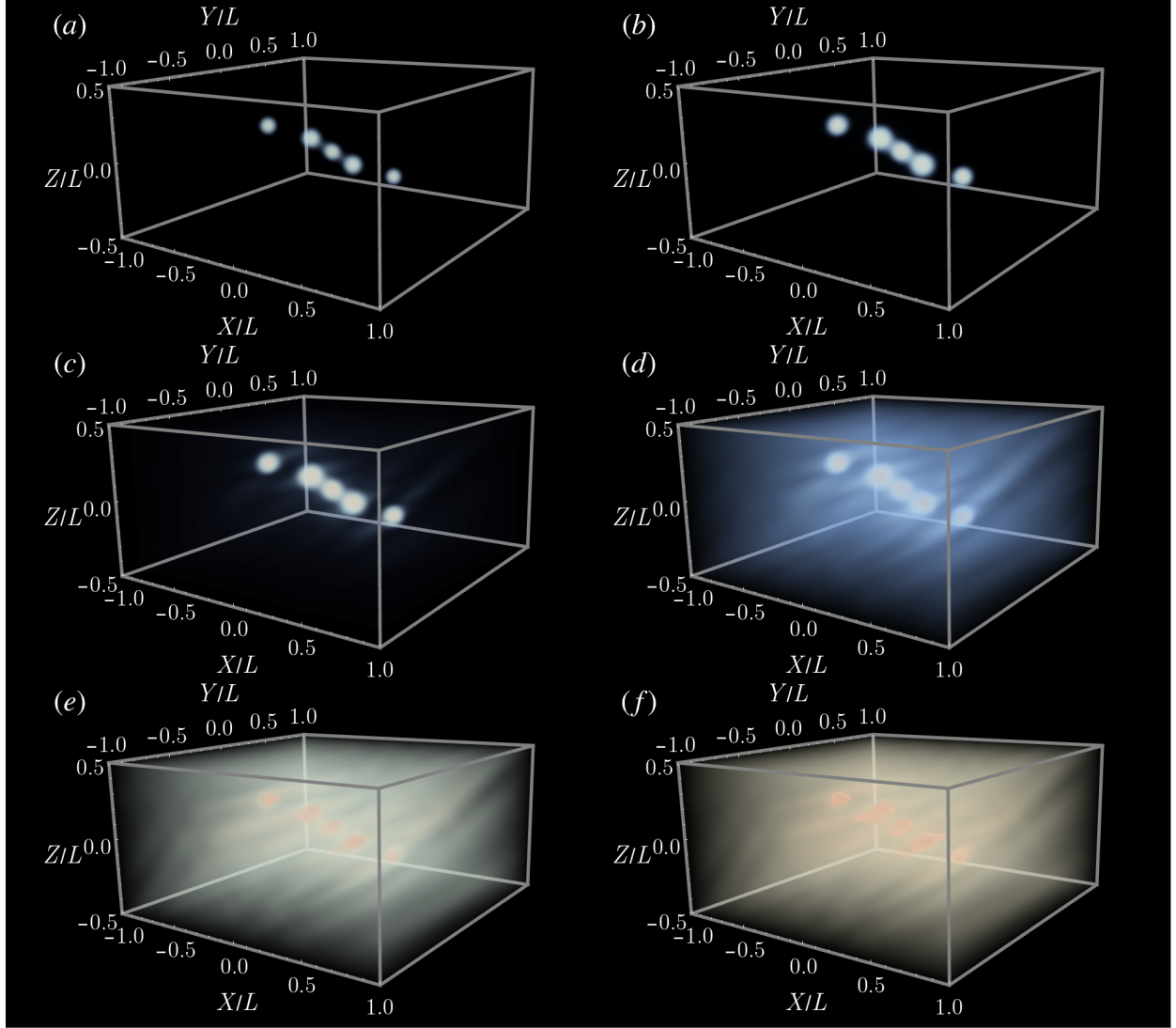


Figure 14: Snapshots of the effective temperature distribution  $\chi(\mathbf{X}, t)$  for a quasi-static simulation. Pure shear deformation is imposed via a domain transformation with an initial condition corresponding to a sequence of blips of elevated  $\chi$  lying roughly along the superdiagonal of the simulation domain. This simulation uses nonperiodic boundary conditions in  $Z$  and is periodic in the  $X$  and  $Y$  directions. The color bar is the same as in Fig. 13. (a)  $t = 0t_s$ ,  $a = 0.75$ ,  $\eta = 1.2$ . (b)  $t = 5 \times 10^3 t_s$ ,  $a = 0.75$ ,  $\eta = 1.2$ . (c)  $t = 10^4 t_s$ ,  $a = 0.75$ ,  $\eta = 1.45$ . (d)  $t = 1.5 \times 10^4 t_s$ ,  $a = 0.75$ ,  $\eta = 1.45$ . (e)  $t = 4 \times 10^5 t_s$ ,  $a = 1.75$ ,  $\eta = 1.75$ . (f)  $t = 4 \times 10^5 t_s$ ,  $a = 1.75$ ,  $\eta = 1.75$ .

The deformation dynamics with nonperiodic boundary conditions are significantly different. By  $t = 8 \times 10^4 t_s$  in Fig. 14(c), diagonal bands have started to nucleate off of each defect in a direction roughly perpendicular to the first bands formed in the periodic simulation. By  $t = 10^5 t_s$  in Fig. 14(d), these diagonal bands have grown more prominent, and an increase in the background  $\chi$  field is seen across the simulation. At times  $t = 2 \times 10^5 t_s$  and  $t = 2.5 \times 10^5 t_s$  in Figs. 14(e) and 14(f) respectively, the qualitative structure remains the same, but the background  $\chi$  field continues to increase. Unlike in the periodic case, true system-spanning shear bands do not fully form in this case.

#### 4.2.2. A randomly fluctuating effective temperature field

In this section, we consider the same sequence of random initializations as in Sec. 4.1.2, but now subject to pure shear deformation. Simulations were performed across values of  $\mu_\chi = 450$  K, 500 K, 525 K, 550 K, 575 K, and 600 K with a fixed value of  $\sigma_\chi = 15$  K. The diffusion length scale was set to  $\frac{3}{2}h$  and the quasi-static timestep was set to  $\Delta t = 200t_s$ . All simulations were conducted on a  $256 \times 256 \times 128$  cell grid with a value of  $\gamma = \frac{1}{2}$ . A pure shear transformation of the form Eq. 34 with  $A(t) = e^{\xi t}$  and a value of  $\xi = 4/t_f$  with  $t_f = 2 \times 10^6 t_s$  so that  $A(t_f) = e^{1/4} \approx 1.284$ . Simulations were performed with fully periodic boundary conditions in all directions; nonperiodic simulations produce qualitatively similar differences as in the case of simple shear.

The results for fully periodic boundary conditions in  $Z$  are shown in Figs. 15–18. The initial conditions are shown in Fig. 15. All simulations undergo an increase in  $\chi$  until the formation of diagonal shear bands begins. Much like the defect simulations seen in the previous section, shear bands nucleate diagonally at roughly  $45^\circ$  angles to the  $X$ – $Y$  plane. As in the simple shear simulations, distributions in  $\chi$  with higher mean values  $\mu_\chi$  have slower dynamics, and take longer to form shear bands. The structural effect of varying  $\mu_\chi$  is most easily seen in Fig. 18. As  $\mu_\chi$  increases, the number of shear bands vastly increases, forming a cross-hatched pattern throughout the domain. The cross-hatching becomes more regular and more finely spaced with higher values of  $\mu_\chi$ .

## Conclusion

In this two-part paper, two variants of a three-dimensional projection method for quasi-static elastoplasticity were developed. These methods are suited for any materials where the hypo-elastoplastic assumption is valid. They are advantageous for stiff materials such as BMGs considered here, which experience small elastic deformation and have high elastic wave speeds. These materials behave quasi-statically in many realistic loading scenarios, making them suitable to the projection method. Numerically, basic explicit discretization methods are limited in their ability to simulate realistic timescales and system sizes in such materials due to timestep restrictions imposed by the CFL condition.

In part I, a family of projection algorithms was presented based on a correspondence between the variables  $(\mathbf{v}, p)$  in incompressible fluid dynamics and the variables  $(\boldsymbol{\sigma}, \mathbf{v})$  in quasi-static hypo-elastoplasticity. This family of methods represents an extension to the two-dimensional algorithm first developed by Rycroft *et al.* [32]. The methods introduce an

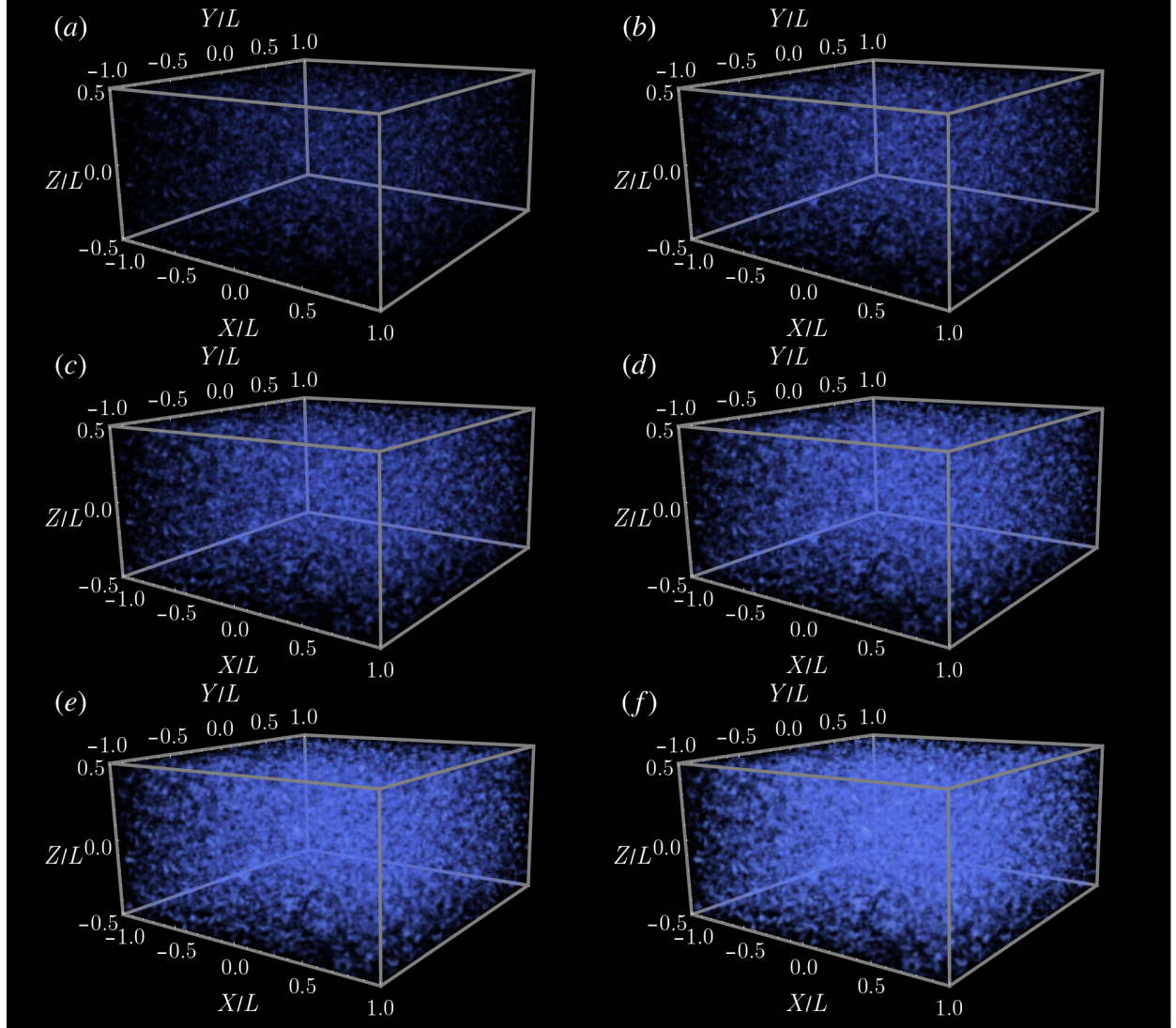


Figure 15: Snapshots of the effective temperature field at  $t = 0t_s$  with a pure shear transformation imposed on the domain. For all plots, a value of  $a = 0.25$  and  $\eta = 1.3$  is used in the opacity function. Figures (a)–(f) have  $\mu_\chi = 450$  K, 500 K, 525 K, 550 K, 575 K, 600 K respectively.

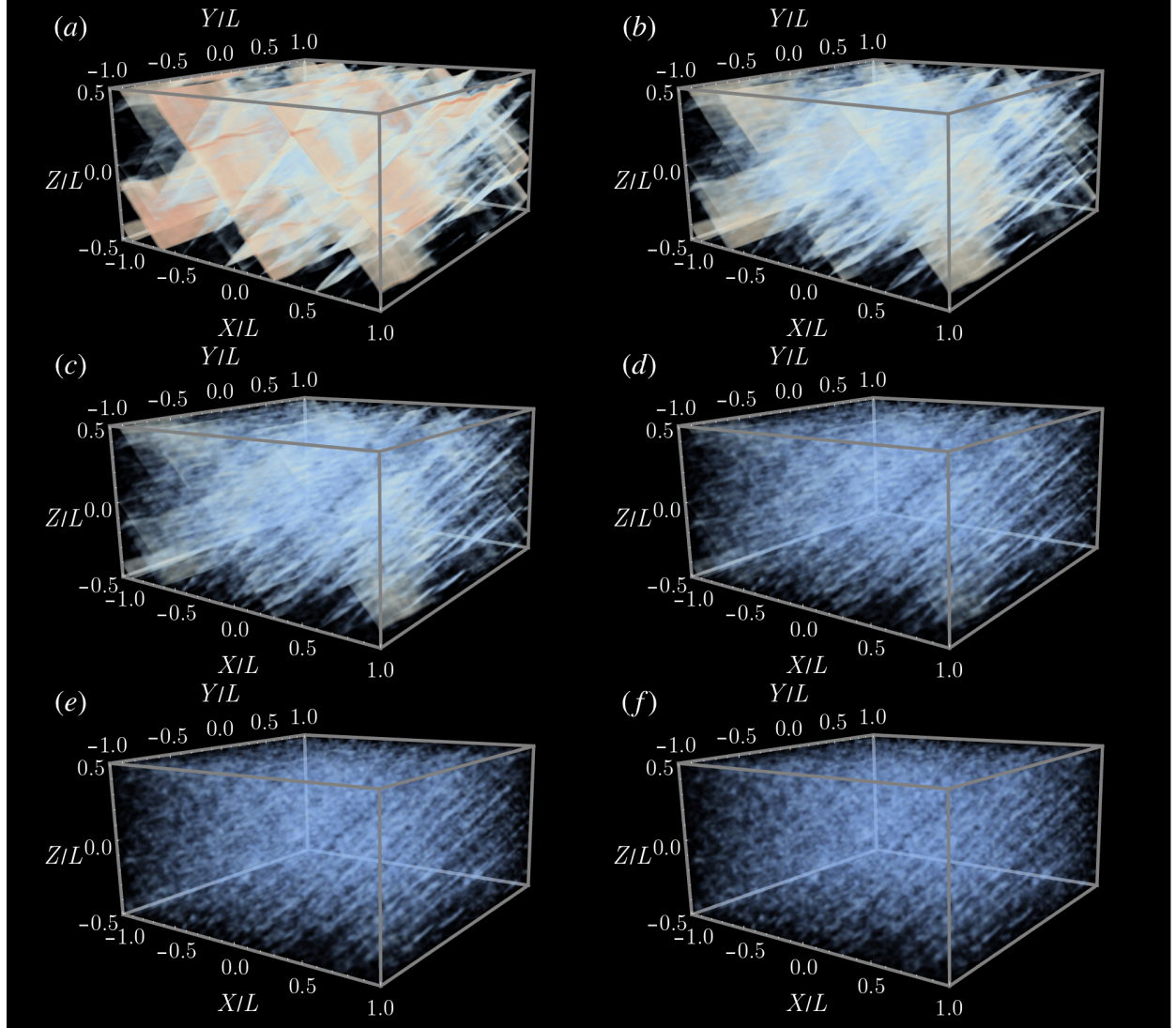


Figure 16: Snapshots of the effective temperature field at  $t = 3 \times 10^5 t_s$  with a pure shear transformation imposed on the domain. For all plots, a value of  $a = 0.55$  and  $\eta = 1.5$  is used in the opacity function. Figures (a)–(f) have  $\mu_\chi = 450$  K, 500 K, 525 K, 550 K, 575 K, 600 K respectively.

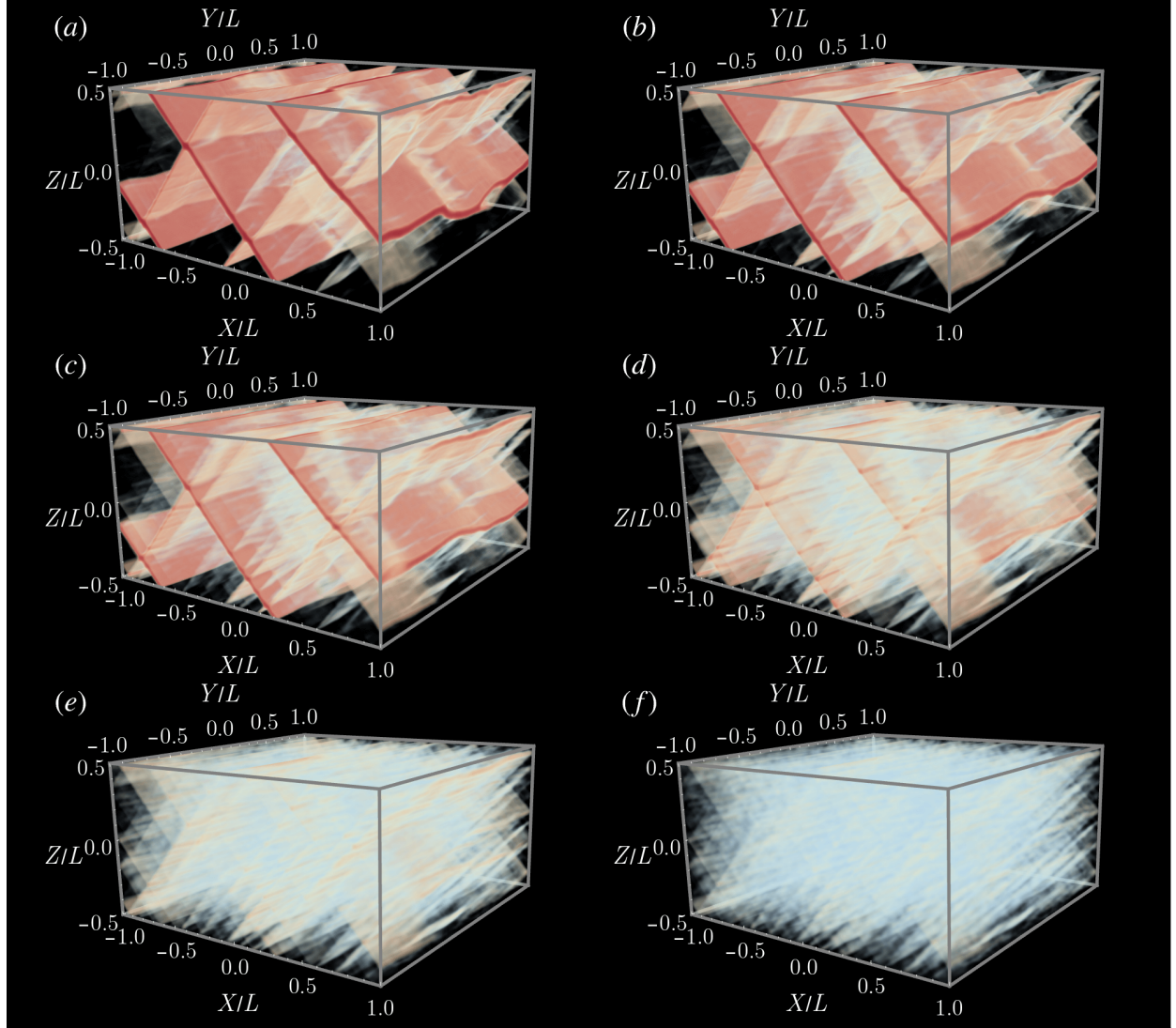


Figure 17: Snapshots of the effective temperature field at  $t = 6 \times 10^5 t_s$  with a pure shear transformation imposed on the domain. For all plots, a value of  $a = 0.75$  and  $\eta = 1.6$  is used in the opacity function. Figures (a)–(f) have  $\mu_\chi = 450$  K, 500 K, 525 K, 550 K, 575 K, 600 K respectively.

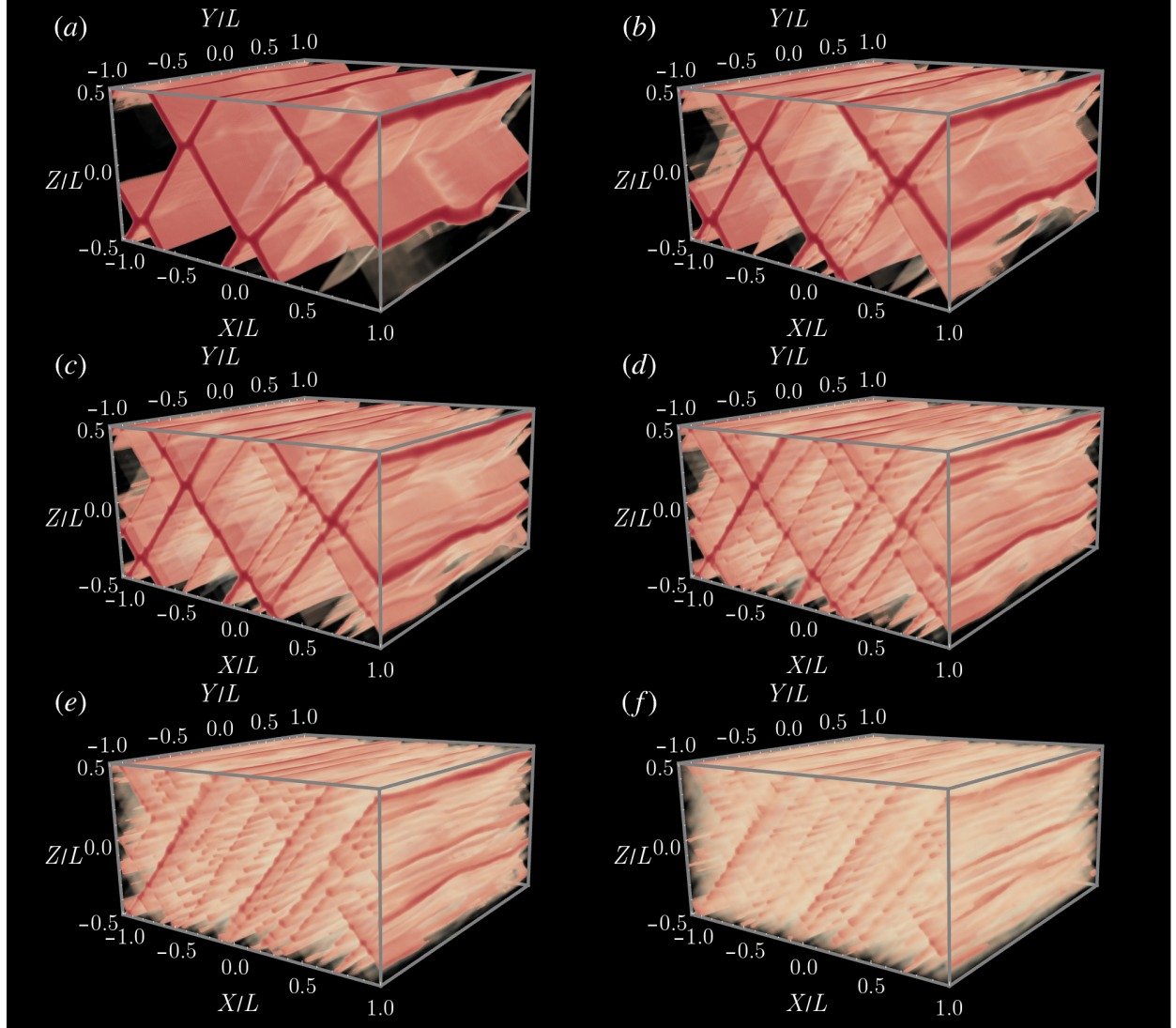


Figure 18: Snapshots of the effective temperature field at  $t = 1.5 \times 10^6 t_s$  with a pure shear transformation imposed on the domain. For all plots, a value of  $a = 1.35$  and  $\eta = 1.5$  is used in the opacity function. Figures (a)–(f) have  $\mu_\chi = 450$  K, 500 K, 525 K, 550 K, 575 K, 600 K respectively.

auxiliary vector field  $\Phi$  that plays a role analogous to the auxiliary scalar field  $\phi$  used in projection algorithms for fluid dynamics. The choice of  $\phi$  and careful consideration of its boundary conditions leads to higher-order projection and gauge methods in fluid dynamics, and we expect similar approaches to generalize to quasi-static hypo-elastoplasticity [46, 47, 48, 49]. Gauge methods couple naturally with discontinuous Galerkin discretization (dG) methods; the theoretical developments in part I thus pave the way for the possibility of similar dG methods in quasi-static hypoelastoplasticity. dG methods are an interesting direction for future work, particularly for resolving the fine-scale features of instabilities such as shear banding in plasticity models.

An implementation of a three-dimensional projection method was developed in C++ and parallelized using domain decomposition and MPI; its specifics are described in part I. To solve the linear system needed for the projection, a new parallel three-dimensional geometric multigrid solver was developed, and some of the computational issues with this solver were discussed. We considered a number of numerical examples within the STZ model of amorphous plasticity to demonstrate the properties of the projection method, but the algorithm is independent of the plasticity model and could be used to investigate plastic deformation in other models. The example simulations were chosen to demonstrate the need for fully three-dimensional simulations, and some unique characteristics of shear banding to three-dimensions were highlighted, such as the development of curvature in shear bands, and the dependence of shear banding structure on the orientation of initial conditions in  $\chi$  with respect to the direction of shear.

In part II, the equations of hypo-elastoplasticity were derived on a fixed reference domain that can be mapped to the physically deforming material through a time-varying linear transformation  $\mathbf{T}(t)$ . The difference between this frame and the Lagrangian frame was demonstrated, and the utility of this frame in implementing complex boundary conditions such as the Lees–Edwards conditions used in molecular dynamics, and pure shear in a fully periodic setting, was demonstrated. The quasi-static projection algorithm was derived in the reference frame and its convergence to the standard method was shown as the level of discretization increases. Several interesting numerical examples were considered in the STZ model of amorphous plasticity. In particular, for a randomly distributed initial condition in the effective temperature field, the dependence of shear banding dynamics on the mean of the distribution was discussed under conditions of simple shear and pure shear.

With the transformation method’s simple implementation of Lees–Edwards conditions, boundary conditions can now be made equivalent in MD and the continuum for the first time. The development of a method to compute a precise matching between atomic configurations in molecular dynamics and effective temperature distributions in continuum simulations is a promising direction of future research. The ability to do so would place internal state variables in plasticity models (such as the effective temperature in the STZ model) on a firmer theoretical footing. In addition, hybrid computational approaches could be developed, where an MD simulation could first be used to compute an initial condition for a significantly larger scale continuum-scale simulation. This type of approach would combine the physical accuracy of MD with the capability of continuum-scale simulations to simulate large system

sizes and long times.

So far our implementations are restricted to cases where the material fills the entire computational domain, and loading is applied via planar boundary conditions, or via the coordinate transformation framework. However, the methods presented here could be generalized to materials with free boundaries, using the level set method [50, 51] to track the material boundary. Methods to do this have already been implemented in two dimensions [52, 53, 32], and the same methods could be used in principle in three dimensions; however, it is a challenging computational task, since it requires extensive modifications to the finite-difference stencils near the material boundary. In particular, since some grid points will lie outside the material, the geometric multigrid method is no longer well-suited for solving the projection step, since it relies on a regular arrangement of grid points. It may be necessary to use algebraic multigrid approaches or Krylov-based linear solvers. Nevertheless this remains a high priority for future work, since it would open up many new directions, such as studying three-dimensional cavitation [54, 55], simulating mode III fracture [56], and predicting the topography of fracture surfaces [57, 58, 59].

## Appendix A. Advective derivative calculation

Consider a scalar field  $\phi(\mathbf{x}, t) = \phi(\mathbf{TX}, t)$ . We can compute the advective derivative of  $\phi$  as follows using the chain rule,

$$\begin{aligned}
\frac{d}{dt}\phi(\mathbf{TX}, t) &= \left( \frac{\partial}{\partial t} + \mathbf{v}^\top \frac{\partial}{\partial \mathbf{x}} \right) \phi(\mathbf{TX}, t) \\
&= \left( \frac{\partial}{\partial t} + \mathbf{v}^\top \mathbf{T}^{-\top} \frac{\partial}{\partial \mathbf{X}} \right) \phi(\mathbf{TX}, t) \\
&= \left( \frac{\partial \mathbf{X}}{\partial t} \right)^\top \frac{\partial}{\partial \mathbf{X}} \phi(\mathbf{TX}, t) + \phi_t(\mathbf{TX}, t) + \mathbf{v}^\top \mathbf{T}^{-\top} \frac{\partial}{\partial \mathbf{X}} \phi(\mathbf{TX}, t) \\
&= \phi_t(\mathbf{TX}, t) + \left( \mathbf{v}^\top \mathbf{T}^{-\top} + \left( \frac{\partial \mathbf{X}}{\partial t} \right)^\top \right) \frac{\partial}{\partial \mathbf{X}} \phi(\mathbf{TX}, t) \\
&= \phi_t(\mathbf{TX}, t) + \left( \mathbf{v}^\top \mathbf{T}^{-\top} + \left( \frac{\partial \mathbf{T}^{-1}}{\partial t} \mathbf{TX} \right)^\top \right) \frac{\partial}{\partial \mathbf{X}} \phi(\mathbf{TX}, t) \\
&= \phi_t(\mathbf{TX}, t) + \mathbf{V}^\top \nabla_{\mathbf{X}} \phi(\mathbf{TX}, t).
\end{aligned} \tag{A.1}$$

In the last line, we have used Eq. 10 and the identity  $\frac{\partial \mathbf{T}^{-1}}{\partial t} = -\mathbf{T}^{-1} \frac{\partial \mathbf{T}}{\partial t} \mathbf{T}^{-1}$ .

## Acknowledgments

The authors thank Eran Bouchbinder and Avraham Moriel (Weizmann Institute of Science) for useful discussions about this work. This work was supported by the National Science Foundation under Grant Nos. DMR-1409560 and DMS-1753203. N. M. Boffi was supported by a Department of Energy Computational Science Graduate Fellowship. C. H. Rycroft

was partially supported by the Applied Mathematics Program of the U.S. DOE Office of Advanced Scientific Computing Research under contract number DE-AC02-05CH11231.

## References

- [1] N. M. Boffi, C. H. Rycroft, *Parallel three-dimensional simulations of quasi-static elastoplastic solids. Part I: Numerical formulation and examples*, arXiv e-prints.
- [2] M. L. Falk, J. S. Langer, *Dynamics of viscoplastic deformation in amorphous solids*, Phys. Rev. E **57** (1998) 7192–7205. doi:[10.1103/PhysRevE.57.7192](https://doi.org/10.1103/PhysRevE.57.7192).
- [3] E. Bouchbinder, J. S. Langer, I. Procaccia, *Athermal shear-transformation-zone theory of amorphous plastic deformation. I. Basic principles*, Phys. Rev. E **75** (2007) 036107. doi:[10.1103/PhysRevE.75.036107](https://doi.org/10.1103/PhysRevE.75.036107).
- [4] J. S. Langer, *Shear-transformation-zone theory of plastic deformation near the glass transition*, Phys. Rev. E **77** (2008) 021502. doi:[10.1103/PhysRevE.77.021502](https://doi.org/10.1103/PhysRevE.77.021502).
- [5] M. P. Allen, D. J. Tidesley (Eds.), *Computer Simulation of Liquids*, Oxford University Press, New York, 1989.
- [6] I. Regev, J. Weber, C. Reichhardt, K. A. Dahmen, T. Lookman, *Reversibility and criticality in amorphous solids*, Nature Communications **6** (2015) 8805. doi:[10.1038/ncomms9805](https://doi.org/10.1038/ncomms9805).
- [7] P. Guan, S. Lu, M. J. B. Spector, P. K. Valavala, M. L. Falk, *Cavitation in Amorphous Solids*, Phys. Rev. Lett. **110** (2013) 185502. doi:[10.1103/PhysRevLett.110.185502](https://doi.org/10.1103/PhysRevLett.110.185502).
- [8] F. Puosi, J. Rottler, J.-L. Barrat, *Time-dependent elastic response to a local shear transformation in amorphous solids*, Phys. Rev. E **89** (2014) 042302. doi:[10.1103/PhysRevE.89.042302](https://doi.org/10.1103/PhysRevE.89.042302).
- [9] D. Hossain, M. Tschopp, D. Ward, J. Bouvard, P. Wang, M. Horstemeyer, *Molecular dynamics simulations of deformation mechanisms of amorphous polyethylene*, Polymer **51** (2010) 6071–6083. doi:[j.polymer.2010.10.009](https://doi.org/j.polymer.2010.10.009).
- [10] <http://lammmps.sandia.gov/>.
- [11] S. Plimpton, *Fast Parallel Algorithms for Short-Range Molecular Dynamics*, Journal of Computational Physics **117** (1995) 1–19. doi:[10.1006/jcph.1995.1039](https://doi.org/10.1006/jcph.1995.1039).
- [12] H. Berendsen, D. van der Spoel, R. van Drunen, *GROMACS: A message-passing parallel molecular dynamics implementation*, Computer Physics Communications **91** (1995) 43–56. doi:[10.1016/0010-4655\(95\)00042-E](https://doi.org/10.1016/0010-4655(95)00042-E).

- [13] C. Maloney, A. Lemaître, *Subextensive Scaling in the Athermal, Quasistatic Limit of Amorphous Matter in Plastic Shear Flow*, Phys. Rev. Lett. **93** (2004) 016001. doi:[10.1103/PhysRevLett.93.016001](https://doi.org/10.1103/PhysRevLett.93.016001).
- [14] C. E. Maloney, A. Lemaître, *Amorphous systems in athermal, quasistatic shear*, Phys. Rev. E **74** (2006) 016118. doi:[10.1103/PhysRevE.74.016118](https://doi.org/10.1103/PhysRevE.74.016118).
- [15] W. Drugan, J. Willis, *A micromechanics-based nonlocal constitutive equation and estimates of representative volume element size for elastic composites*, Journal of the Mechanics and Physics of Solids **44** (1996) 497–524. doi:[10.1016/0022-5096\(96\)00007-5](https://doi.org/10.1016/0022-5096(96)00007-5).
- [16] J. Chaboche, *A review of some plasticity and viscoplasticity constitutive theories*, International Journal of Plasticity **24** (2008) 1642–1693, special Issue in Honor of Jean-Louis Chaboche. doi:[10.1016/j.ijplas.2008.03.009](https://doi.org/10.1016/j.ijplas.2008.03.009).
- [17] C. Song, P. Wang, H. A. Makse, *Experimental measurement of an effective temperature for jammed granular materials*, Proceedings of the National Academy of Sciences **102** (2005) 2299–2304. doi:[10.1073/pnas.0409911102](https://doi.org/10.1073/pnas.0409911102).
- [18] M. Dijkstra, R. van Roij, R. Evans, *Phase diagram of highly asymmetric binary hard-sphere mixtures*, Phys. Rev. E **59** (1999) 5744–5771. doi:[10.1103/PhysRevE.59.5744](https://doi.org/10.1103/PhysRevE.59.5744).
- [19] P. G. Bolhuis, A. A. Louis, J. P. Hansen, *Many-body interactions and correlations in coarse-grained descriptions of polymer solutions*, Phys. Rev. E **64** (2001) 021801. doi:[10.1103/PhysRevE.64.021801](https://doi.org/10.1103/PhysRevE.64.021801).
- [20] E. R. Homer, C. A. Schuh, *Three-dimensional shear transformation zone dynamics model for amorphous metals*, Modelling and Simulation in Materials Science and Engineering **18** (2010) 065009. doi:[10.1088/0965-0393/18/6/065009](https://doi.org/10.1088/0965-0393/18/6/065009).
- [21] E. R. Homer, C. A. Schuh, *Mesoscale modeling of amorphous metals by shear transformation zone dynamics*, Acta Materialia **57** (2009) 2823–2833. doi:[10.1016/j.actamat.2009.02.035](https://doi.org/10.1016/j.actamat.2009.02.035).
- [22] V. V. Bulatov, A. S. Argon, *A stochastic model for continuum elasto-plastic behavior. I. Numerical approach and strain localization*, Modelling and Simulation in Materials Science and Engineering **2** (1994) 167–184. doi:[10.1088/0965-0393/2/2/001](https://doi.org/10.1088/0965-0393/2/2/001).
- [23] V. Bulatov, A. Argon, *A stochastic model for continuum elasto-plastic behavior. III. Plasticity in ordered versus disordered solids*, Modelling and Simulation in Materials Science and Engineering **2** (1999) 203. doi:[10.1088/0965-0393/2/2/003](https://doi.org/10.1088/0965-0393/2/2/003).
- [24] A. W. Lees, S. F. Edwards, *The computer study of transport processes under extreme conditions*, Journal of Physics C: Solid State Physics **5** (1972) 1921.

- [25] A. Kraynik, D. Reinelt, *Extensional motions of spatially periodic lattices*, International Journal of Multiphase Flow **18** (1992) 1045–1059. [doi:10.1016/0301-9322\(92\)90074-Q](https://doi.org/10.1016/0301-9322(92)90074-Q).
- [26] B. D. Todd, P. J. Daivis, *Nonequilibrium Molecular Dynamics Simulations of Planar Elongational Flow with Spatially and Temporally Periodic Boundary Conditions*, Phys. Rev. Lett. **81** (1998) 1118–1121. [doi:10.1103/PhysRevLett.81.1118](https://doi.org/10.1103/PhysRevLett.81.1118).
- [27] B. Todd, P. J. Daivis, *A new algorithm for unrestricted duration nonequilibrium molecular dynamics simulations of planar elongational flow*, Computer Physics Communications **117** (1999) 191–199. [doi:10.1016/S0010-4655\(98\)00178-7](https://doi.org/10.1016/S0010-4655(98)00178-7).
- [28] A. Baranyai, P. T. Cummings, *Steady state simulation of planar elongation flow by nonequilibrium molecular dynamics*, The Journal of Chemical Physics **110** (1999) 42–45. [arXiv:https://doi.org/10.1063/1.478082](https://arxiv.org/https://doi.org/10.1063/1.478082), [doi:10.1063/1.478082](https://doi.org/10.1063/1.478082).
- [29] M. Dobson, *Periodic boundary conditions for long-time nonequilibrium molecular dynamics simulations of incompressible flows*, The Journal of Chemical Physics **141** (2014) 184103. [doi:10.1063/1.4901276](https://doi.org/10.1063/1.4901276).
- [30] J. W. Demmel, Applied Numerical Linear Algebra, SIAM, 1997.
- [31] W. L. Briggs, V. E. Henson, S. F. McCormick, A Multigrid Tutorial: Second Edition, Society for Industrial and Applied Mathematics, Philadelphia, PA, USA, 2000.
- [32] C. H. Rycroft, Y. Sui, E. Bouchbinder, *An Eulerian projection method for quasi-static elastoplasticity*, Journal of Computational Physics **300** (2015) 136–166. [doi:10.1016/j.jcp.2015.06.046](https://doi.org/10.1016/j.jcp.2015.06.046).
- [33] A. R. Hinkle, C. H. Rycroft, M. D. Shield, M. L. Falk, *Coarse graining atomistic simulations of plastically deforming amorphous solids*, Phys. Rev. E **95** (2017) 053001. [doi:10.1103/PhysRevE.95.053001](https://doi.org/10.1103/PhysRevE.95.053001).
- [34] M. E. Gurtin, E. Fried, L. Anand, The Mechanics and Thermodynamics of Continua, Cambridge University Press, Cambridge, 2010.
- [35] M. L. Falk, J. Langer, *Deformation and Failure of Amorphous, Solidlike Materials*, Annual Review of Condensed Matter Physics **2** (2011) 353–373. [doi:10.1146/annurev-conmatphys-062910-140452](https://doi.org/10.1146/annurev-conmatphys-062910-140452).
- [36] E. Bouchbinder, J. S. Langer, I. Procaccia, *Athermal shear-transformation-zone theory of amorphous plastic deformation. I. Basic principles*, Phys. Rev. E **75** (2007) 036107. [doi:10.1103/PhysRevE.75.036107](https://doi.org/10.1103/PhysRevE.75.036107).
- [37] M. L. Manning, J. S. Langer, J. M. Carlson, *Strain localization in a shear transformation zone model for amorphous solids*, Phys. Rev. E **76** (2007) 056106. [doi:10.1103/PhysRevE.76.056106](https://doi.org/10.1103/PhysRevE.76.056106).

- [38] J. S. Langer, M. L. Manning, *Steady-state, effective-temperature dynamics in a glassy material*, Phys. Rev. E **76** (2007) 056107. doi:[10.1103/PhysRevE.76.056107](https://doi.org/10.1103/PhysRevE.76.056107).
- [39] M. L. Manning, E. G. Daub, J. S. Langer, J. M. Carlson, *Rate-dependent shear bands in a shear-transformation-zone model of amorphous solids*, Phys. Rev. E **79** (2009) 016110. doi:[10.1103/PhysRevE.79.016110](https://doi.org/10.1103/PhysRevE.79.016110).
- [40] E. Bouchbinder, J. S. Langer, *Nonequilibrium thermodynamics of driven amorphous materials. II. Effective-temperature theory*, Phys. Rev. E **80** (2009) 031132. doi:[10.1103/PhysRevE.80.031132](https://doi.org/10.1103/PhysRevE.80.031132).
- [41] Y. Shi, M. L. Falk, *Strain Localization and Percolation of Stable Structure in Amorphous Solids*, Phys. Rev. Lett. **95** (2005) 095502. doi:[10.1103/PhysRevLett.95.095502](https://doi.org/10.1103/PhysRevLett.95.095502).
- [42] C. Chen, M. Gao, C. Wang, W.-H. Wang, T.-C. Wang, *Fracture behaviors under pure shear loading in bulk metallic glasses*, Scientific Reports **6**.
- [43] Z. Zhang, J. Eckert, L. Schultz, *Difference in compressive and tensile fracture mechanisms of Zr<sub>59</sub>Cu<sub>20</sub>Al<sub>10</sub>Ni<sub>8</sub>Ti<sub>3</sub> bulk metallic glass*, Acta Materialia **51** (2003) 1167–1179. doi:[10.1016/S1359-6454\(02\)00521-9](https://doi.org/10.1016/S1359-6454(02)00521-9).
- [44] W. J. Wright, R. Saha, W. D. Nix, *Deformation Mechanisms of the Zr<sub>40</sub>Ti<sub>14</sub>Ni<sub>10</sub>Cu<sub>12</sub>Be<sub>24</sub> Bulk Metallic Glass*, Materials Transaction **42** (2001) 642–649. doi:[10.2320/matertrans.42.642](https://doi.org/10.2320/matertrans.42.642).
- [45] Y. H. Sun, D. Louzguine-Luzgin, S. Ketov, A. Greer, *Pure shear stress reversal on a Cu-based bulk metallic glass reveals a Bauschinger-type effect*, Journal of Alloys and Compounds **615** (2014) S75–S78. doi:[10.1016/j.jallcom.2013.11.104](https://doi.org/10.1016/j.jallcom.2013.11.104).
- [46] D. L. Brown, R. Cortez, M. L. Minion, *Accurate Projection Methods for the Incompressible Navier–Stokes Equations*, J. Comput. Phys. **168** (2001) 464–499. doi:[10.1006/jcph.2001.6715](https://doi.org/10.1006/jcph.2001.6715).
- [47] R. Saye, *Implicit mesh discontinuous Galerkin methods and interfacial gauge methods for high-order accurate interface dynamics, with applications to surface tension dynamics, rigid body fluidstructure interaction, and free surface flow: Part I*, Journal of Computational Physics **344** (2017) 647–682. doi:[10.1016/j.jcp.2017.04.076](https://doi.org/10.1016/j.jcp.2017.04.076).
- [48] R. Saye, *Implicit mesh discontinuous Galerkin methods and interfacial gauge methods for high-order accurate interface dynamics, with applications to surface tension dynamics, rigid body fluidstructure interaction, and free surface flow: Part II*, Journal of Computational Physics **344** (2017) 683–723. doi:[10.1016/j.jcp.2017.05.003](https://doi.org/10.1016/j.jcp.2017.05.003).
- [49] R. Saye, *Interfacial gauge methods for incompressible fluid dynamics*, Science Advances **2**. doi:[10.1126/sciadv.1501869](https://doi.org/10.1126/sciadv.1501869).

- [50] J. A. Sethian, *Level Set Methods and Fast Marching Methods*, Cambridge University Press, 1996.
- [51] S. J. Osher, R. P. Fedkiw, *Level Set Methods and Dynamic Implicit Surfaces*, Springer-Verlag, New York, 2003.
- [52] C. H. Rycroft, F. Gibou, *Simulations of a stretching bar using a plasticity model from the shear transformation zone theory*, Journal of Computational Physics **231** (2012) 2155–2179. doi:[10.1016/j.jcp.2011.10.009](https://doi.org/10.1016/j.jcp.2011.10.009).
- [53] C. H. Rycroft, E. Bouchbinder, *Fracture Toughness of Metallic Glasses: Annealing-induced embrittlement*, Phys. Rev. Lett. **109** (2012) 194301. doi:[10.1103/PhysRevLett.109.194301](https://doi.org/10.1103/PhysRevLett.109.194301).
- [54] E. Bouchbinder, T.-S. Lo, I. Procaccia, E. Shtilerman, *Stability of an expanding circular cavity and the failure of amorphous solids*, Phys. Rev. E **78** (2008) 026124. doi:[10.1103/PhysRevE.78.026124](https://doi.org/10.1103/PhysRevE.78.026124).
- [55] M. L. Falk, *Molecular-dynamics study of ductile and brittle fracture in model noncrystalline solids*, Phys. Rev. B **60** (1999) 7062–7070. doi:[10.1103/PhysRevB.60.7062](https://doi.org/10.1103/PhysRevB.60.7062).
- [56] A. Karma, D. A. Kessler, H. Levine, *Phase-Field Model of Mode III Dynamic Fracture*, Phys. Rev. Lett. **87** (2001) 045501. doi:[10.1103/PhysRevLett.87.045501](https://doi.org/10.1103/PhysRevLett.87.045501).
- [57] P. Lowhaphandu, L. Ludrosky, S. Montgomery, J. Lewandowski, *Deformation and fracture toughness of a bulk amorphous Zr–Ti–Ni–Cu–Be alloy*, Intermetallics **8** (2000) 487–492. doi:[10.1016/S0966-9795\(99\)00137-5](https://doi.org/10.1016/S0966-9795(99)00137-5).
- [58] Z. F. Zhang, J. Eckert, L. Schultz, *Fatigue and fracture behavior of bulk metallic glass*, Metallurgical and Materials Transactions A **35** (2004) 3489–3498. doi:[10.1007/s11661-004-0186-5](https://doi.org/10.1007/s11661-004-0186-5).
- [59] R. Raghavan, P. Murali, U. Ramamurty, *On factors influencing the ductile-to-brittle transition in a bulk metallic glass*, Acta Materialia **57** (2009) 3332–3340. doi:[10.1016/j.actamat.2009.03.047](https://doi.org/10.1016/j.actamat.2009.03.047).